THESIS

A SIMPLIFIED APPROACH TO UNDERSTANDING BOUNDARY LAYER STRUCTURE IMPACTS ON TROPICAL CYCLONE INTENSITY

Submitted by

Eleanor G. Delap

Department of Atmospheric Science

In partial fulfillment of the requirements

For the Degree of Master of Science

Colorado State University

Fort Collins, Colorado

Fall 2018

Master's Committee:

Advisor: Michael M. Bell

Eric D. Maloney
Subhas Karen Venayagamoorthy

ABSTRACT

A SIMPLIFIED APPROACH TO UNDERSTANDING BOUNDARY LAYER STRUCTURE IMPACTS ON TROPICAL CYCLONE INTENSITY

The relationship between tropical cyclone boundary layer (TCBL) structure and tropical cyclone (TC) intensity change is difficult to understand due to limited observations of the complex, non-linear interactions at both the top and bottom boundaries of the TCBL. Consequently, there are debates on how the TCBL interacts with surface friction and how these interactions affect TC intensity change.

To begin to address these questions, a conceptual framework of how axisymmetric dynamics within the TCBL can impact TC intensity change is developed from first principles in the form of a new, simple logistic growth equation (LGE). Although this LGE bears some similarities to the operational LGE Model (LGEM; DeMaria 2009), the difference is that our growth-limiting term incorporates TCBL structure and surface drag. The carrying capacity of the LGE—termed the instantaneous logistic potential intensity (ILPI) in this study—is used to explore the relationship between TCBL structure and TC intensity. The LGE is also further solved for the drag coefficient (C_D) to explore the relationships between it and both TCBL structure and TC intensity.

The validity of this new LGE framework is then explored in idealized numerical modeling using the axisymmetric version of Cloud Model 1 (CM1; Bryan and Fritsch 2002). Results show that CM1 exhibits changes to TCBL structure and TC intensity that are consistent with the LGE framework. Sensitivity of these results to the turbulent mixing lengths, L_h and L_v, are also explored, and general LGE relationships still hold as C_D is increased. Finally, the LGE framework is applied to observations, and initial C_D retrievals indicate that while this new method is low compared to Bell et al. (2012), they are still plausible estimates.

ACKNOWLEDGMENTS

This research is supported by the ONR Young Investigator Program awards N000141613033 and N000141712230.

I would like to thank my advisor, Michael Bell, for the opportunity to pursue this research. I would also like to thank my family, friends, and the rest of the Bell research group for their support and comradery. Finally, I would like to thank my soon-to-be husband, Mike Casas, for all of his sacrifices, patience, support, and encouragement as I transitioned from my undergraduate program at Valpo to graduate school in Hawaii, and then again when I transferred from Hawaii to Colorado State.

This thesis is typeset in LaTeX using a document class created by Leif Anderson and modified by Christopher Slocum.

TABLE OF CONTENTS

LIST OF FIGURES

CHAPTER 1

Introduction

The tropical cyclone boundary layer (TCBL) is known to be important to the tropical cyclone (TC) intensification process, due in part to its ability to converge angular momentum with frictionally forced inflow (e.g. Smith et al. 2009). In addition, the TBCL is also the primary source of enthalpy and sink of momentum in a TC (Bell et al. 2012). However, the exact magnitude of the momentum sink is unknown because the exact magnitude of the surface drag coefficient (C_D) for TC wind speeds is unknown, and many different surface wind speed–C_D relationships have been proposed for surface wind speeds over 30 m s^{-1} (Fig. 1.1). These proposed relationships range from monotonically increasing drag (e.g. Charnock 1955; Large and Pond 1981), to nearly invariant drag (e.g. Emanuel 2003; Black et al. 2007), to decreasing drag as surface wind speeds continue to increase over 30 m s^{-1} (e.g. Powell et al. 2003; Donelan et al. 2004; Makin 2005; Jarosz et al. 2007; Hsu et al. 2017; Soloviev et al. 2017). However, few observations of C_D exist to confirm or deny these relationships due to the many hazards associated with collecting in situ data, such as extreme turbulence and sea salt corrosion in research aircraft engines. Additionally, while unmanned aircraft systems are an emerging technology that can obtain in situ C_D estimates, they are currently rather expensive expendable measurement systems that can only provide C_D estimates for a limited amount of time and for a small spatial domain within a TC. As a result, methods that can be used to remotely retrieve C_D within the TCBL from a safer distance are helpful to reduce the uncertainty of the drag coefficient.

In addition to the uncertainty in the magnitude of C_D for TC wind speeds, there are also uncertainties in the effects of drag on TCBL structure and TC intensity change. While surface drag is known to influence TC intensity change and intensification rates, there is no consensus on whether increased drag helps or hinders TC intensification. Theoretically, maximum potential intensity theory first proposed in Emanuel (1986) shows that increased drag results in a weaker maximum potential intensity. However, seemingly counter to this hypothesis, some numerical simulations have shown that TCs actually intensify faster and reach higher intensities with increased surface drag (Bao et al. 2012; Green and Zhang 2014). Other studies argue that this increase in intensification rates is only valid for a specific range of values of C_D (Montgomery et al. 2010; Smith et al. 2014), and that the increased torque of radial inflow can only offset the increased sink of momentum up to a certain extent of surface drag. However, this proposed dependence on the magnitude of C_D implies complex, nonlinear relationships associated

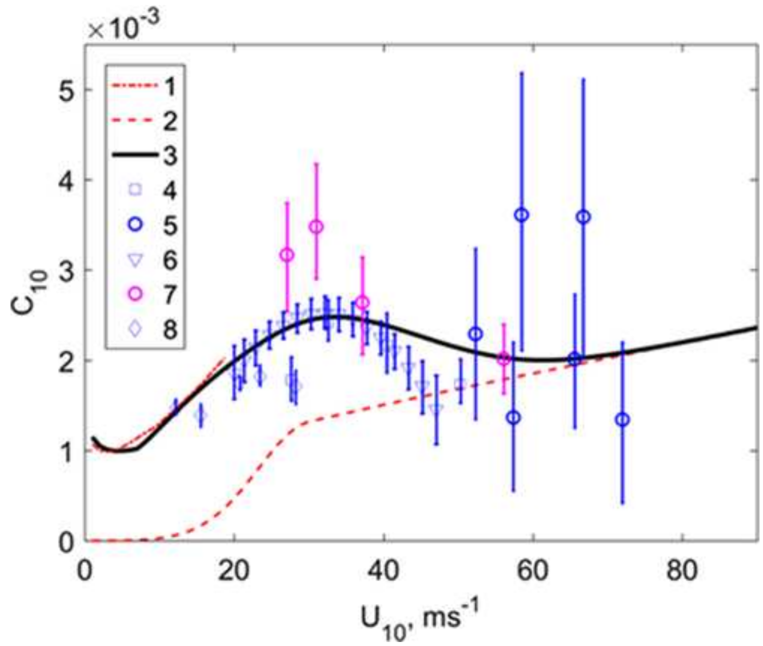

FIG. 1.1. Examples of the uncertainty of the 10-m drag coefficient at large wind speeds. Reprinted from Soloviev et al. (2017), where the lines and symbols indicate: 1, COARE 3.0 algorithm (Fairall et al. 2003); 2, two-phase layer parameterization (Soloviev and Lukas 2010); 3, unified parameterization (Soloviev et al. 2014); 4, dropwindsondes (Powell et al. 2003); 5, angular momentum conservation (Bell et al. 2012); 6, upper ocean current response (Jarosz et al. 2007); 7, upper ocean current response (Hsu et al. 2017); and 8, dropwindsondes (Black et al. 2007). Error bars indicate confidence intervals of observed C_D.

with TCBL structure, and only qualitative relationships were described. Therefore, as a result of these seemingly contrary hypotheses and complex structural interactions, a need for a simplified nonlinear theory that unifies surface drag, TCBL structure, and TC intensity becomes apparent.

Finally, in addition to its physical and meteorological importance, the TCBL is also intrinsically important to society because it is the part of a TC that directly interacts with the Earth's surface and causes loss of life, damage to infrastructure, and economic hardship. As a result, having a better understanding of the TCBL structure and intensity are needed for improving TC forecasts, disaster preparations, and structural engineering.

However, despite its clear importance, the TCBL is one of the least understood parts of a TC, and even simply defining the height of the TCBL has proven to be challenging (Zhang et al. 2011). Therefore, to better understand the TCBL, this study seeks to develop a simple conceptual framework to better understand how the structure of the TCBL changes in response to a change in the surface drag coefficient, and how the adjusted TCBL structure relates to TC intensification.

1.1 Defining the TCBL

While the TCBL is generally thought as the lowest $1-2$ km of the atmosphere within a TC that directly interacts with the Earth's surface through surface-induced turbulent fluxes, more precisely defining it has proven to be difficult. Early TCBL studies (e.g. Moss and Merceret 1976) typically used a thermodynamic definition: the near-surface layer of nearly constant, or "well-mixed," potential temperature. This line of thinking stems from planetary boundary layer (PBL) conventions that originate from the 1968 Kansas Experiment, which provided observational evidence of Monin-Obhukov similarity theory in that most turbulent fluxes within the well-mixed layer tend to zero at approximately the same height as a subsidence-induced capping inversion (Kaimal and Wyngaard 1990). In addition, vertical profiles in the clear-air regions of the outer rainbands of Tropical Storm Eloise (1975) seemed to confirm that the well-mixed layer also corresponded well to the true height of the TCBL (Moss and Merceret 1976). Thus, there was no initial reason to suspect that the inner-core TCBL might have fundamentally different structure than either the clear-air regions of the outer rainbands or the PBL.

However, more recent studies suggest that defining the TCBL as the near-surface well-mixed layer underestimates the true TCBL height by roughly half, especially in the inner-core region (Fig. 1.2; Kepert et al. 2016; Zhang et al. 2011, 2009). The reason for the height discrepancy has been shown to be primarily due to the strong diabatic heat release from the overlying condensation in clouds (Kepert et al. 2016). Since the height of the TCBL should encompass all of the surface-induced turbulent fluxes, these studies recommend using a dynamically-based definition instead, such as the height of the surface inflow layer. However, using the surface inflow depth as a proxy for the TCBL depth is still an unsatisfactory definition—especially in the inner-core region of TCs where TCBL air is lofted into the overlying convection and in asymmetric TCs that may not have surface inflow in all quadrants (Zhang et al. 2011; Smith and Montgomery 2010).

Another definition used in the literature is the height of the maximum tangential wind speed (e.g. Bryan and Rotunno 2009), since it is usually unambiguous and near the top of the TCBL (Fig. 1.2b). However, this definition is not without its faults, either. Typically, the maximum tangential wind speed is found within the inflow layer at a height of approximately 25% of the peak radial inflow (Zhang et al. 2011). Since the height of the inflow layer best approximates the height of the TCBL, this usually means that using the height of the tangential wind speed maximum as a proxy for the TCBL height also underestimates the true vertical extent of the TCBL, although the underestimate is much less severe than when using the well-mixed layer height.

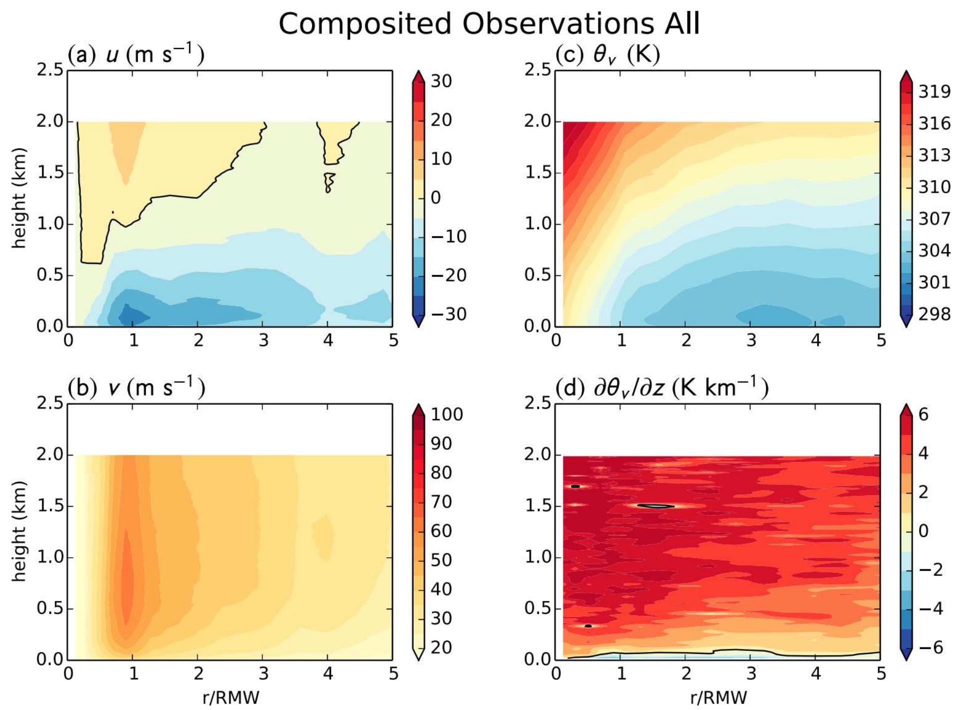

FIG. 1.2. Dropsonde composite TCBL structure reprinted from Kepert et al. (2016), where the parameters are: (a) radial velocity (m s^{-1}); (b) tangential velocity (m s^{-1}); (c) virtual potential temperature (K); and (d) stability (K km^{-1}).

In this study, the height of the maximum tangential wind will be regarded as being near the top of the TCBL, and its relationship to the top of the radial inflow layer will be explored. While the interactions between the other different height definitions are also interesting, further exploring them is beyond the scope of this study.

1.2 Relationships between TCBL Structure, Surface Drag, and TC Intensification

In addition to difficulties with simply defining the TCBL, the relationship between TCBL structure and TC intensity is also not well understood. While the TCBL plays a significant part in modulating TC intensity (Smith and Montgomery 2010; Smith et al. 2009), nonlinear interactions at both the top and bottom boundaries of the TCBL obfuscate the physical mechanisms responsible for influencing TC intensity change.

At the top of the TCBL, it is not fully clear how the TCBL interacts with the mean vortex above it. While a key assumption of traditional PBL theory is that turbulent momentum transport becomes negligible at the top of the PBL, this assumption does not hold for all regions of the TCBL. In particular, the TCBL underneath the eyewall violates this assumption because the entire eyewall is highly turbulent due to large horizontal and vertical wind shear (Lorsolo et al. 2010; Smith and Montgomery 2010). This means that assuming boundary conditions at the top of the TCBL that have turbulent flow transitioning to laminar, balanced flow above the TCBL are inherently flawed for highly turbulent regions.

Another example of this assumption in a TC framework would be to assume that the top of the TCBL is in gradient wind balance. By assuming gradient wind balance at the top of the TCBL leads to wind exiting the TCBL almost vertically into the eyewall convection and that the TCBL cannot directly determine the flow above it, which may not be true (Smith and Montgomery 2010). Since flow above the TCBL is typically assumed to be in gradient wind balance, there is an unclear dynamic relationship between the agradient flow in the TCBL and the flow above it.

At the bottom of the TCBL, a different set of nonlinear interactions emerge. This is because the ocean surface has different structural characteristics with respect to different surface wind speeds. For low wind speeds under 20 m s^{-1}, there is generally a direct relationship between increasing surface wind speeds, increasing wave heights, and C_D. While factors such as wave age and cross-swell may introduce some variability in terms of geometric roughness and surface drag, the direct relationship between surface wind speed and drag is generally well-described by the relationships of Charnock (1955) and Large and Pond (1981). The primary difference between the two relationships is that Charnock's relation is relating the drag coefficient to the friction velocity and gravity, and Large and Pond's relation is an empirical fit to observed 10-m winds. These relationships have been then extrapolated to TC-strength wind speeds because there are few direct observations of C_D for surface winds over 20 m s^{-1}, but extrapolation yields rather large magnitudes of $C_D \geq 5 \times 10^{-3}$ for Category 5 TCs on the Saffir-Simpson scale.

Recent observational evidence from the Coupled Boundary Layer Air–Sea Transfer Experiment (CBLAST) and laboratory experiments indicate that as surface wind speeds are increased beyond approximately $23 - 33$ m s^{-1}, the surface drag coefficient may actually either remain nearly constant at $C_D \approx 2.4 \times 10^{-3}$ or even decrease after reaching a critical wind speed in this range (Bell et al. 2012; Black et al. 2007; Donelan et al. 2004; Holthuijsen et al. 2012; Makin 2005; Powell et al. 2003). This means that the monotonically increasing relations that were previously discussed are likely no longer valid for tropical storm surface wind speeds and above, because these relationships would severely overestimate the actual drag coefficient. In fact, the overestimates could be so large that TCs above 50 m s^{-1} (Category 3+ on the Saffir-Simpson scale) would experience too much surface friction to exist (Donelan et al. 2004; Emanuel 1995). Since TCs regularly attain maximum surface wind speeds well over 50 m s^{-1} annually around the globe, the surface drag coefficient must therefore have a nonlinear relationship with the surface wind speed. Currently, models such as the Cloud Model 1 (CM1) employ a wind-drag relationship that generally follow the Charnock relation up to approximately 25 m s^{-1}, and then remain either constant or slightly decrease with wind speeds beyond that. However, the exact nature of this nonlinear relationship between surface wind speed and C_D is still unknown.

The prevailing physical explanation for why the drag coefficient has a nonlinear relationship with surface wind speed is that the ocean surface characteristics markedly change around 25 m s^{-1}. As surface wind speeds increase within the range of $0-25$ m s^{-1}, locally-generated waves become bigger, steeper, and the appearance of whitecaps atop spilling breaker waves steadily increase in surface area coverage (Holthuijsen et al. 2012). This increase in breaking waves for this wind speed range is generally well described by the Charnock relation (Makin 2005), since the geometric roughness and surface drag are increasing with increasing surface wind speed (Black et al. 1986).

However, as surface wind speeds increase from $25-40$ m s^{-1}, they start becoming strong enough to mechanically shear off the whitecaps from the tops of the spilling breakers, and the separated whitecaps become spume. As a result, the ocean surface becomes an emulsion of sea spray, foam, and bubble streaks in which the boundary between the ocean and atmosphere becomes ambiguous (Holthuijsen et al. 2012; Emanuel 2003). This surface emulsion has the net effect of becoming a slip layer that keeps the drag coefficient nearly constant as the surface wind speeds continue to increase, but there are multiple factors that contribute towards the slip-layer effect in this wind speed regime.

The first factor is that foam and bubble streaks act to reduce the geometric roughness of the ocean surface, which then also limits the surface drag. However, there is also a nonlinear relationship between wind speed and foam coverage, because the presence of TC-induced swell modulates the amount of foam present. This TC-induced swell crosses the locally-generated waves at different angles in different regions around the TC, and the angle of swell that modulates foam coverage the most is the cross swell angled at about 90° from the locally-generated waves. The reason for cross-swell having the largest effect on foam coverage is because when the swell and local waves are perpendicular, the wave crest length is shortened, the whitecap width is reduced, and the foam width is reduced (Holthuijsen et al. 2012), which results in less foam and a higher average drag coefficient. In addition, since the swell originated as locally-generated waves from the TC at an earlier time, the swell is also a product of TC storm motion. As a result, the TC-generated swell leads to a subtle azimuthal variation of the surface drag coefficient around the TC.

The second factor is that sea spray acts as a suspension layer, which theory suggests acts to accelerate the near-surface flow (Makin 2005). Since the sea spray originates from the sheared off whitecaps—which are most prevalent on the short, steep waves—the depth of the sea spray suspension layer is likely shorter than the significant wave height (Makin 2005). However, the depth of the suspension layer also likely depends on surface wind speed. This is because within the $25-40$ m s^{-1} surface wind speed range, the sea spray is mostly landing in the troughs or backs of downwind waves (Holthuijsen et al. 2012). However the ocean surface becomes progressively more obscured by the sea spray as winds increase within this range.

Finally, as surface wind speeds continue to increase beyond approximately 40 m s^{-1}, the ocean surface starts to enter into "whiteout" conditions, in which there is a fast-moving layer of mist and sea spray that visually obscures the foamy ocean surface (Holthuijsen et al. 2012). Within this whiteout regime, the surface drag coefficient is especially uncertain, and may even substantially decrease. Other studies posit that beyond 60 m s^{-1}, C_D may even increase with increasing wind speed again (Soloviev and Lukas 2010; Soloviev et al. 2017).

While the surface drag coefficient for large wind speeds over the open ocean is uncertain, knowing the exact surface drag coefficient is essential because it has been shown to affect overall TC intensity and rate of change in numerical weather prediction models. However, in addition to uncertainty in the magnitude of C_D, there is also uncertainty as to how C_D affects TC intensity. This is because depending on the model setup, the drag coefficient can either positively or negatively affect TC intensity and intensification rates as C_D is increased.

Early studies showed that as the surface drag coefficient is increased within a TC, there is a monotonic decrease in the maximum possible axisymmetric tangential wind speed (e.g. Emanuel 1986, 1995). The physical reasoning for the inverse relationship between surface drag and maximum potential intensity (MPI) of TCs was that the ocean acts as a momentum sink, which acts to remove kinetic energy from the atmosphere. However, even though the ocean acts as a momentum sink for TCs, it is also acts as the primary source of enthalpy that sustains TCs, such that there is a direct relationship between the enthalpy coefficient, C_K, and MPI. As a result, there is an inverse relationship between the enthalpy coefficient and the drag coefficient that is important in determining the maximum potential TC intensity, such that C_K/C_D. While the two coefficients are not directly related, the square of the surface wind speed is proportional to this ratio.

In contrast, some newer studies show that there is a direct relationship between increasing surface drag and maximum TC intensity (e.g. Bao et al. 2012; Green and Zhang 2014). One explanation for this direct relationship is that they keep C_D and C_K equal such that the ratio between them stays a constant 1. Therefore, while there is an increased momentum sink, there is also an enhanced latent heat flux, which counteracts the increased surface friction and then results in deeper convection. However, these results are most prominent when C_D and C_K are increased in the outer core (Bao et al. 2012; Green and Zhang 2014).

A third C_D–max intensity relationship has also been proposed in recent literature: increasing C_D increases TC intensity up to a critical value of C_D, above which there is either a limited or negative impact on maximum TC intensity (Montgomery et al. 2010; Smith et al. 2014). This is because there is a positive effect from the frictional torque that increases inflow and convergence of angular momentum, but also a negative effect from the frictional loss of momentum. Thus, the net effect of C_D depends on the magnitude of the wind speed, such that lower surface wind speeds will converge more angular momentum than is lost to friction, and higher surface wind speeds lose more angular momentum to friction than is converged.

While the results of Montgomery et al. (2010) and Smith et al. (2014) appear to be in direct contrast to the previous proposed relationship, one possible reason for this difference is how the enthalpy exchange coefficient C_K is treated. While Bao et al. (2012) and Green and Zhang (2014) kept C_D and C_K constant and equal to each other as C_D was increased, Montgomery et al. (2010) and Smith et al. (2014) kept C_K a set constant value as C_D was increased. Thus, the enthalpy coefficient could potentially either enhance or reverse the effects of C_D depending on how it is treated in a numerical simulation. While slightly different simulation time lengths could also be a slight factor towards the result differences, all of the simulations were $85-120$ hr long, and none of the simulations were run to a quasi-steady state.

In contrast, a likely reason for the discrepancy of results between Emanuel (1995) and Montgomery et al. (2010) is the short simulation time length of Montgomery et al. (2010) when compared to Emanuel (1995) (Bryan 2013). While Emanuel (1995) describes a relationship between C_D and MPI with respect to a steady-state solution, Montgomery et al. (2010) describe results from the current maximum intensity of simulations after four days. As a result of the differing definitions used, Montgomery et al. (2010) was able to show that there is an inconsistency between the relationship between C_D and maximum *potential* intensity and the relationship between C_D and maximum *current* intensity. Therefore, this inconsistency highlights the utility of a relationship between C_D and the current maximum TC intensity at any given time.

In addition to examining effects of C_D on TC intensity, Montgomery et al. (2010) and Smith et al. (2014) also qualitatively discuss changes in TCBL structure as C_D is increased in numerical simulations. They note that as C_D is increased, the radius of maximum wind decreases and the depth of the inflow layer increases. In addition, they saw that the maximum near-surface inflow magnitude increased as C_D was increased, which was attributed to an increase in the frictional torque. They also noted that an increase in the frictional torque also leads to a reduction in the near-surface tangential wind speed. However, while qualitative relationships were described, no quantitative relationship was offered between C_D and TCBL structure.

1.3 Thesis Overview

Many challenges pertaining to multiple nonlinear aspects of the TCBL and the drag coefficient have been described. However, in outlining these many challenges, what becomes clear is that the TCBL is a unique part of the atmosphere in which there is still much to learn. As a result, this study seeks to develop a simple conceptual framework to understand how the structure of the TCBL changes in response to a change in the surface drag coefficient, and how the adjusted TCBL structure relates to TC intensification.

To develop this simple conceptual framework, a logistic growth equation (LGE) will be derived from first principles. An empirically-derived LGE has previously been used successfully to model and forecast TC intensity in the Logistic Growth Equation Model (LGEM; DeMaria 2009). In LGEM, a series of large-scale variables are used as predictors in the growth and decay terms of an empirically-derived LGE. However, since LGEM primarily incorporates large-scale predictors, it does not directly include small-scale TCBL terms. Therefore, there is an opportunity to derive a new, simple, and nonlinear LGE that incorporates TCBL structure and surface drag.

Thus, by including TCBL structure and surface drag in this new LGE, the three primary research questions of this study can be examined:

(1) How does TCBL structure relate to current and potential TC intensity?

(2) How does TCBL structure quantitatively relate to the drag coefficient?

(3) Can this LGE framework retrieve the drag coefficient from observations?

To answer these questions, new relations will be developed that will be tested numerically with the Cloud Model 1 (CM1; Bryan and Fritsch 2002) and observationally with Hurricane Joaquin (2015), Hurricane Fabian (2003), and Hurricane Isabel (2003) (Bell et al. 2016, 2012). In Chapter 2, the new LGE and subsequent relations will be derived, the model setup will be described, and the observational dataset and analysis technique will be detailed for Hurricane Joaquin. In Chapter 3, the validity and sensitivity of the new relationships using both CM1 and observations will be presented, and in Chapter 4, some concluding remarks will be discussed.

CHAPTER 2

Data & Methods

2.1 Derivations

2.1.1 Deriving the LGE

To derive the new LGE from first principles, we will start with the tangential wind component of the momentum equation in cylindrical coordinates. We will then assume that the vortex is axisymmetric, such that the momentum equation becomes:

$$\frac{\partial \bar{v}}{\partial t} + \bar{u}\frac{\partial \bar{v}}{\partial r} + \bar{w}\frac{\partial \bar{v}}{\partial z} + \frac{\bar{u}\bar{v}}{r} + f\bar{u} = F_{\lambda}, \tag{2.1}$$

where the terms in order are the: Eulerian time tendency, the radial advection, the vertical advection, the centrifugal acceleration, the Coriolis acceleration, and the net nonconservative forces. The overbars denote axisymmetric averages, but will be dropped hereafter for clarity. We will then solve at the specific tangential wind maximum, v_{max}, where the remaining advection terms are zero because the partial derivatives are zero by definition of a global maximum. Therefore, at v_{max}, the momentum equation simplifies to:

$$\frac{\partial v_{max}}{\partial t} + \frac{u_m v_{max}}{r_m} + f u_m = F_{\lambda}, \tag{2.2}$$

where the subscript m denotes the value of the variable at the location of v_{max}. Since v_{max} has previously been shown to typically be located near the top of the near-surface frictional inflow layer (Zhang et al. 2011), this also means that the terms with a subscript m reside in the TCBL. Thus, this study will be relating TCBL structure with v_{max} and its rate of change.

We can then assume that $(u_m v_{max})/(r_m) >> f u_m$ for the case of a developed TC, and then solve for $\partial v_{max}/\partial t$, such that:

$$\frac{\partial v_{max}}{\partial t} = -\frac{u_m v_{max}}{r_m} + F_{\lambda}. \tag{2.3}$$

We can then assume that F_{λ} is predominately characterized by the surface stress τ, such that:

$$\frac{\partial v_{max}}{\partial t} = -\frac{u_m v_{max}}{r_m} + \frac{\partial \tau_z}{\partial z} + \frac{\partial \tau_r}{\partial r}. \tag{2.4}$$

where the subscripts r and z denote the radial and vertical components of the surface stress, respectively. Further assuming that $\partial \tau_z / \partial z >> \partial \tau_r / \partial r$, the expression then becomes:

$$\frac{\partial v_{max}}{\partial t} = -\frac{u_m v_{max}}{r_m} + \frac{\partial \tau_z}{\partial z}, \tag{2.5}$$

where τ_z can be represented by the bulk aerodynamic formula $\tau_z = C_D \bar{\rho} ||\mathbf{V_{10}}|| v_{10}$ at the surface, such that:

$$\tau_s \equiv \frac{\partial \tau_z}{\partial z} = \frac{0 - C_D \bar{\rho} ||\mathbf{V_{10}}|| v_{10}}{z_m - 0}, \tag{2.6}$$

where $||\mathbf{V_{10}}||$ is the magnitude of the total horizontal 10-m wind, which is defined as $||\mathbf{V_{10}}|| \equiv \sqrt{u_{10}^2 + v_{10}^2}$; v_{10} is the 10-m tangential wind; and ρ is the TCBL-average air density. In addition, Eq. 2.6 also assumes that turbulence goes to zero at z_m. While this is not the most realistic assumption in the eyewall region since it assumes that the surface fluxes vary linearly with height and that the TCBL force associated with stress is constant, making these assumptions allow for greater simplicity, and this study seeks to determine the appropriateness of assuming this simplified TCBL structure.

Solving per unit density, and introducing a scaling factor $\alpha = v_{10}/v_{max}$ that scales the maximum tangential wind speed down to the 10-m tangential wind speed, this simplifies to:

$$\tau_s = -\frac{C_D ||\mathbf{V_{10}}|| \alpha v_{max}}{z_m}. \tag{2.7}$$

Assuming that $v_{10}^2 >> u_{10}^2$ for $||\mathbf{V_{10}}||$ at r_m, simplifies $||\mathbf{V_{10}}||$ to:

$$||\mathbf{V_{10}}|| \approx v_{10} = \alpha v_{max}. \tag{2.8}$$

Therefore, combining 2.7 and 2.8 yields:

$$\tau_s = -\frac{\alpha^2 C_D v_{max}^2}{z_m}. \tag{2.9}$$

By substituting 2.9 into 2.5, we obtain the new LGE:

$$\boxed{\frac{\partial v_{max}}{\partial t} = \left(\frac{-u_m}{r_m} \right) v_{max} - \left(\frac{\alpha^2 C_D}{z_m} \right) v_{max}^2}, \tag{2.10}$$

where we further assume that the parenthetical terms are approximately constant on short time scales. The first term on the right-hand side of the LGE represents the growth term because it has to be positive for a TC to intensify. Plus, since v_{max} is typically near the top of the near-surface frictional inflow layer, this generally means that $u_m < 0$ and the growth term coefficient is positive. The second term on the right-hand side of the LGE represents the decay term because it is negative definite, and shows that higher magnitudes of C_D will result in greater decay. However, C_D also has effects on the other TCBL structural parameters, and the relationships between these parameters is a focus of this study.

2.1.2 Deriving ILPI

As in DeMaria (2009), we can assign general coefficients $\kappa \equiv (-u_m)/(r_m)$ and $\mu \equiv (\alpha^2 C_D)/(z_m)$ and rewrite 2.10 as:

$$\frac{\partial v_{max}}{\partial t} = \kappa v_{max} - \mu v_{max}^2. \tag{2.11}$$

In addition, we can also define the ratio between the two coefficients—which is termed the instantaneous logarithmic potential intensity ($ILPI$)—such that:

$$ILPI \equiv \frac{\kappa}{\mu} = \frac{-u_m}{r_m}\left(\frac{\alpha^2 C_D}{z_m}\right)^{-1}, \tag{2.12}$$

which simplifies to:

$$\boxed{ILPI \equiv \frac{(-u_m) z_m}{\alpha^2 r_m C_D}}. \tag{2.13}$$

$ILPI$, which is equivalent to the "carrying capacity" of the LGE, can further be defined as a vortex-centric maximum potential intensity. Since the LGE is derived with respect to v_{max}, ILPI can be used to assess the instantaneous TC vortex development potential from TCBL structure. However, note that since $ILPI$ does not incorporate any environmental parameters, it is different than *a priori* maximum potential intensity metrics (e.g. Emanuel 1986). Thus, $ILPI$ is used in this study to avoid confusion.

To better understand $ILPI$, the conceptual relationships between the TCBL structural parameters and $ILPI$ are depicted in Fig. 2.1. If an arbitrary TC has an initial TCBL structure as shown in Fig. 2.1a, then changes to the TCBL parameters in $ILPI$ will result in TC intensity change, and these changes are consistent within the context of angular momentum. Increasing $(-u_m)$ will converge angular momentum surfaces towards the TC center, which will intensify v_{max} if its location doesn't change (Fig. 2.1b). If the height of v_{max} increases without a change to the initial angular momentum surfaces, then v_{max} will be further to the right of its original angular momentum surface, and consequently intensify (Fig. 2.1c). If α^2 is decreased such that the difference between v_{max} and v_{10} is increased, then the slope of the angular momentum surfaces will be decreased and less vertical, which will again put v_{max} to the right of its original angular momentum surface (Fig. 2.1d). If v_{max} is kept on its original angular momentum surface but r_m is decreased, then v_{max} will increase (Fig. 2.1e). Finally, if the angular momentum at the top of the TCBL is kept the same but C_D is decreased such that less momentum is transferred to the

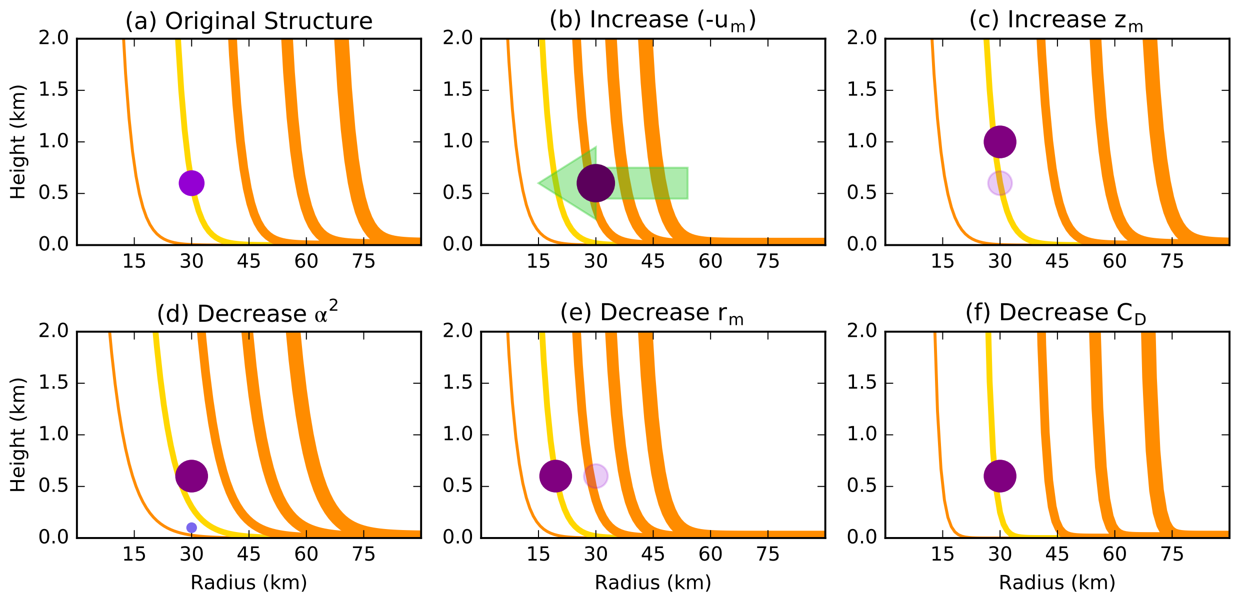

FIG. 2.1. Conceptual schematic showing how each term effects $ILPI$ if the others are held constant. The opaque purple point represents the location of v_{max}, and it becomes darker the more its magnitude is increased. Transparent purple points for r_m and z_m represent the original location prior to adjusting the position of v_{max}. The blue point in (d) represents that the magnitude of v_{10} has been decreased from its magnitude in the original structure in (a). Orange and gold curves denote angular momentum surfaces, where increasing line thickness represents increasing magnitudes of angular momentum. The gold curves represent the "original" angular momentum surface to highlight its relative location to v_{max}.

ocean, then v_{max} will again be to the right of its original angular momentum surface and thus increase (Fig. 2.1f).

To better understand how $ILPI$ relates to the LGE, Fig. 2.2 demonstrates the typical LGE properties of Eq. 2.10 when $ILPI$ is held constant at 100 m s^{-1}. The maximum intensification rate occurs at the inflection point

$$\left(\frac{r_m}{-u_m}\ln\left(\frac{ILPI - v_0}{v_0}\right), \frac{ILPI}{2}\right) \tag{2.14}$$

by definition of general LGE properties, and that if there is no initial tangential wind, then a TC will not develop in this framework.

However, an important note is that $ILPI$ is not a constant; rather, it is rapidly fluctuating with time because the TCBL is constantly adjusting to perturbations from its top and bottom boundaries. Nevertheless, Fig. 2.2 shows that an initial v_{max} (hereafter v_0) adjusts towards $ILPI$ with time, regardless if it is initially less than or greater than $ILPI$. Therefore, $ILPI$ can be thought as an “attractor,” and the magnitude of $ILPI$ relative to v_0 indicates if a TC is instantaneously intensifying or weakening.

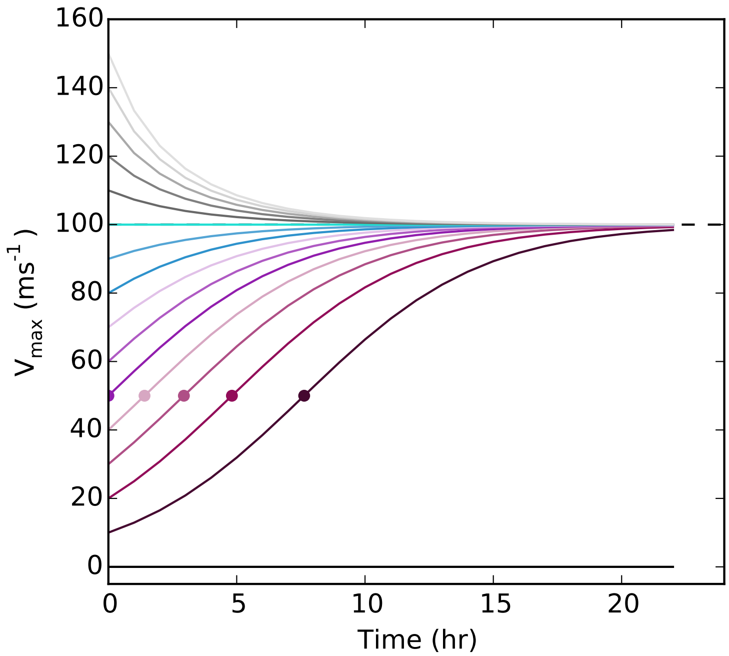

FIG. 2.2. Arbitrary logistic growth curves with initial tangential winds varying every 10 m s^{-1}. Solid curves represent the axisymmetric maximum tangential wind, and the black, dashed line represents the $ILPI = 100$ m s^{-1} for the solid curves. Scatter points denote the maximum intensification rate, which is given by Eq. 2.14.

Eq. 2.13 also reveals that the only parameter that can realistically change the sign of $ILPI$ is u_m since the location of v_{max} may instantaneously lie in the radial outflow just above the TCBL, and the effect of a changing u_m on $ILPI$ is demonstrated in Fig. 2.3. However, while $ILPI$ can become negative, the tangential wind does not, and it asymptotes to 0 m s^{-1} instead of becoming negative. Additionally, if $0 < ILPI < v_0$, then the TC would weaken as well in this conceptual framework.

2.1.3 Deriving the Integral Form of C_D

In addition to simply defining $ILPI$ and examining the effects of TCBL structure on instantaneous TC potential intensity, we can also solve the LGE in Eq. 2.10 to derive a theoretical equation that relates C_D to TCBL structure. First, Eq. 2.10 can be integrated and solved for v_{max}, such that

$$v_{max} = \frac{ILPI}{1 + Ae^{\frac{u_m}{r_m}t}}, \qquad \text{where } A = \frac{ILPI - v_0}{v_0}. \tag{2.15}$$

Then, Eq. 2.15 can be rearranged and solved for C_D, such that

$$\boxed{C_D = \frac{(-u_m)z_m}{\alpha^2 r_m v_0}\left(\frac{\frac{v_0}{v_{max}} - e^{\frac{u_m}{r_m}t}}{1 - e^{\frac{u_m}{r_m}t}}\right)}, \tag{2.16}$$

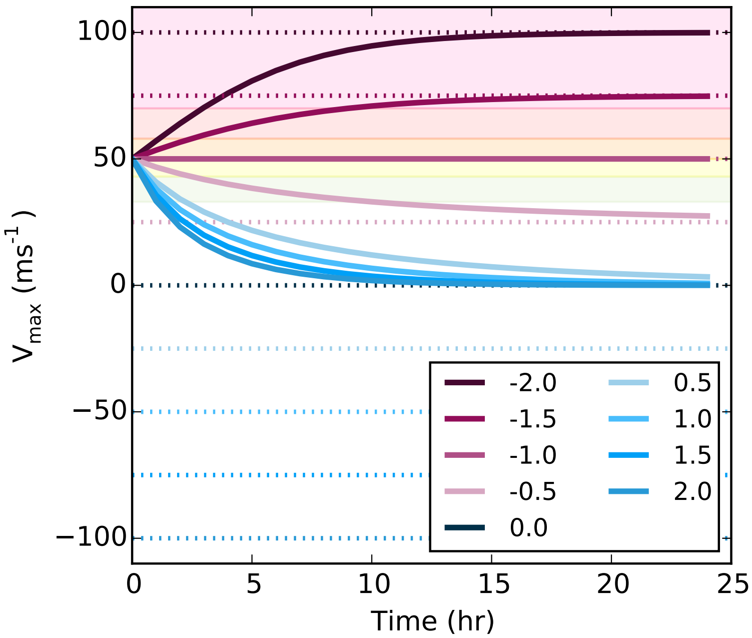

FIG. 2.3. Arbitrary logistic growth curves (solid) and corresponding $ILPI$ values (dotted) where the radial wind is varied from -2 m s^{-1} to 2 m s^{-1}. Inflow is denoted by purple, outflow is denoted by blue, and a radial wind of 0 m s^{-1} results in an undefined curve. Shading denotes TC intensity according to the Saffir-Simpson scale.

where Eq. 2.16 will be referred to as the Integral Form of C_D retrievals, and the parenthetical term within it will be referred as the time tendency term. Eq. 2.16 shows that C_D is inversely proportional to the maximum attainable tangential wind speed, and that the decay rate is governed by the ratio of u_m and r_m.

2.1.4 Deriving the Differential Form of C_D

To get a simpler, more intuitive form of the drag coefficient equation, we can instead start with the LGE in Eq. 2.10, and directly solve for C_D, such that

$$\frac{z_m}{\alpha^2 v_{max}^2}\frac{\partial v_{max}}{\partial t} = \frac{(-u_m)z_m}{\alpha^2 r_m v_{max}} - C_D, \tag{2.17}$$

If we assume that $[(z_m)/(\alpha^2 v_{max}^2)](\partial v_{max}/\partial t) \approx 0$, then C_D becomes

$$\boxed{C_D \approx \frac{(-u_m)z_m}{\alpha^2 r_m v_{max}}}, \tag{2.18}$$

where Eq. 2.18 will be referred to as the Differential Form of C_D retrievals. In addition, Eq. 2.18 is also the limit of Eq. 2.16 as time goes to infinity. As a result, Eq. 2.18 does not have the time tendency term.

Therefore, the elimination of a time dependence allows for a more direct relationship between C_D and TCBL structure, and a comparison between the two forms of C_D retrievals will be explored.

Overall, in deriving the new LGE, $ILPI$, and both forms of C_D, this study assumes that:

(1) the developed TC is axisymmetric

(2) the centrifugal acceleration is much larger than the acceleration due to Coriolis in a TC

(3) the net nonconservative forces can be characterized by the surface stress

(4) the surface stress can be described by the bulk aerodynamic formula

(5) turbulence tends to zero at z_m

(6) the 10-m wind speed is dominated by the tangential wind component

(7) and the time scales of interest are short enough that the TCBL structure is nearly constant

In deriving the Differential Form of C_D, an approximate steady-state assumption is also applied.

2.2 Experimental Designs

To test these new relations, several experiments are performed with the Cloud Model 1 (CM1; Bryan and Fritsch 2002). The first test is the control experiment (hereafter Experiment 1), and it demonstrates the initial results when using all of the default axisymmetric TC settings of v.18 CM1. These settings are: 4 km radial grid point spacing; 59 vertical grid levels, with 11 levels below 2 km; a sea surface temperature of 301.15 K; Morrison Double-Moment microphysics scheme (Morrison et al. 2009); and a 2D Smagorinsky-type diffusion scheme, in which the vertical turbulent mixing length, L_v, is set to 100 m, and the horizontal turbulent mixing length is a linear formulation from 100 m at a surface pressure of 1015 hPa to 1000 m at a surface pressure of 900 hPa. Experiment 1 allows C_D to vary with wind speed until $C_D = 2.4 \times 10^{-3}$, and further details on the PBL scheme and the specific C_D formulation in CM1 can be found in Bryan et al. (2017). The magnitude of the enthalpy exchange coefficient, C_K, is set constant at $C_K = 1.0 \times 10^{-3}$.

However, instead of letting C_D vary with wind speed as in Experiment 1, Experiment 2 forces C_D and C_K to be constant and equal to each other within CM1, which allows for testing the new relations with a greater number of C_D values. Therefore, Experiment 2 has eight simulations that are run from $C_D = C_K = (0.5 - 4.5) \times 10^{-3}$ at 0.5×10^{-3} intervals, where the "$\times 10^{-3}$" notation is dropped hereafter for clarity and conciseness. Finally, to better compare the Experiment 2 results with the results of Experiments 1 and 3, all other settings besides C_D and C_K remain the same.

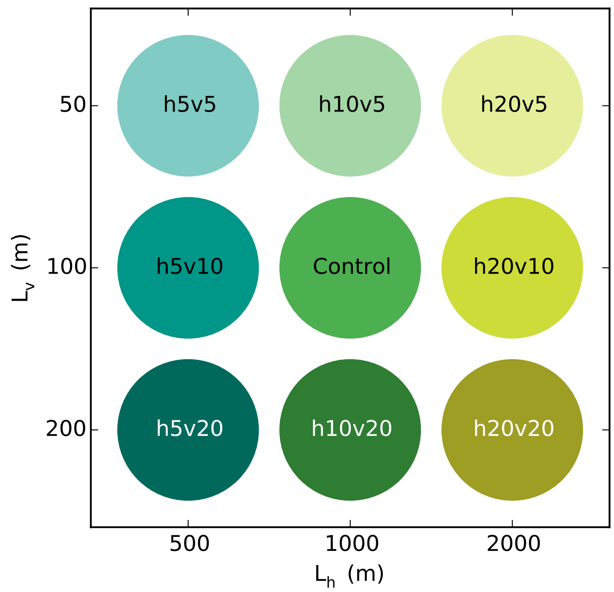

FIG. 2.4. Experimental design of testing u_m sensitivity to L_h and L_v, where: the top row is half the default L_v, the bottom row is double the default L_v, the first column is half the default L_h, and the last column is double the default L_v.

Since TCBL structure has previously been shown to be sensitive to turbulent mixing lengths (e.g. Bryan 2012; Rotunno and Bryan 2012), Experiment 3 examines the sensitivity of these results to the horizontal and vertical turbulent mixing lengths, L_h and L_v, respectively. To test the sensitivity, L_h and L_v are either halved, doubled, or kept at their default values, as shown in Fig. 2.4. The drag and enthalpy coefficients are set to a constant $C_D = C_K = 2.5$ across all simulations to most closely represent the maximum C_D in the Experiment 1, and the control run for Experiment 3 is the Experiment 2 $C_D = 2.5$ simulation.

2.3 Observations

At the end of this study, the CM1 results will be compared with the previously published analyses of Hurricanes Fabian and Isabel (2003) (Bell et al. 2012), as well as with new observational analyses of Hurricane Joaquin (2015) that utilized dropsonde data from the 2015 Tropical Cyclone Intensity field experiment (TCI; Doyle et al. 2017). Hurricane Joaquin had unusual extratropical origins and was designated a tropical depression on 28 Sep 2015, and quickly developed into a major hurricane by 1 Oct 2015. During that time, Hurricane Joaquin was nearly stationary but moving slightly southeastward towards the Bahamas because there was a strong upper-level ridge over the western Atlantic. However, on 2 Oct 2015, an upper-level trough came over the US East Coast (Fig. 2.5a), and began to break down the ridge. This allowed Hurricane Joaquin to do a hairpin turn, and start propagating to the north northeast. This was also the strongest Hurricane Joaquin was during the four days in which TCI operated, according to

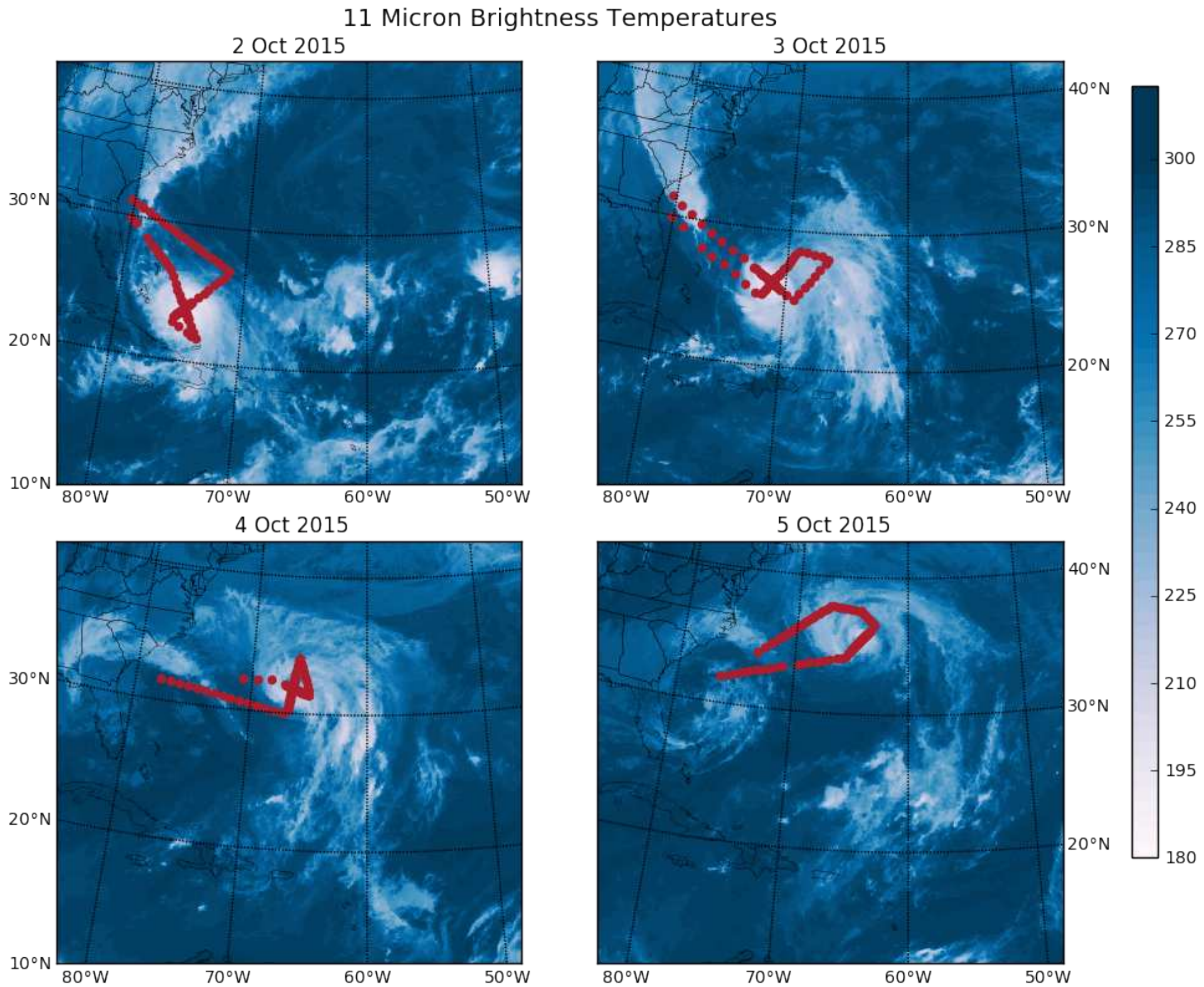

FIG. 2.5. HDSS dropsonde locations and 11 micron brightness temperatures showing the synoptic environment of Hurricane Joaquin from 2 – 5 Oct 2015.

the National Hurricane Center best track. On 3 Oct 2015 (Fig. 2.5b), there were significant interactions with the trough, and Hurricane Joaquin started accelerating to the northeast. Joaquin also temporarily intensified, but then significantly weakened by the end of the day. On 4 Oct 2015 (Fig. 2.5c), Hurricane Joaquin lost its major hurricane status, but was still a hurricane. On 5 Oct 2015 (Fig. 2.5d), Hurricane Joaquin was still weakening, and was beginning to show signs of extratropical transition, which was completed four days later.

The data used from Hurricane Joaquin were the high definition sounding system (HDSS) dropsondes that were deployed as a part of TCI (Bell et al. 2016). While TCI also sampled three other systems in that hurricane season—Ex-Tropical Storm Erika, Hurricane Marty, and Hurricane Patricia—their radial passes for dropsondes were not nearly as perpendicular as those deployed in Hurricane Joaquin, and not all TC quadrants were sampled. Thus, their axisymmetric analyses were not as representative of the true axisymmetric structure, and they will not be examined in this study.

A significant benefit of using the TCI dropsondes is that they are the first HDSS dropsondes deployed in a field campaign; thus, they have unprecedented radial resolution along the flight path (Doyle et al. 2017). Therefore, axisymmetric, cylindrical dropsonde analyses were created using a spline-based, data-assimilation tool (SAMURAI; Bell et al. 2012).

In SAMURAI, the dropsonde data locations and spatial densities for all four flights into Hurricane Joaquin are shown in Figs. 2.6–2.7. The axisymmetric resolution on all flights allowed for an analysis radial grid spacing of 5 km and a vertical grid spacing of 50 m, where the analysis domain extended radially from the TC center to 200 km and vertically from the surface to 5 km. In addition, the axisymmetric resolution was sufficient to forgo needing a background field. A radial Gaussian filter of $6\Delta x$ and a vertical Gaussian filter of $2\Delta x$ were used to interpolate across data gaps. TC center positions and storm motion were first estimated from NHC Best Track locations, and then manually adjusted to better align with the approximate wind center.

Looking closer at the specific data distribution, Fig. 2.6 shows the SAMURAI-adjusted azimuthal locations of the dropsondes after accounting for the storm motion during the TCI flights. Three of the four TCI flights on $2-4$ Oct 2015 had two radial passes into Hurricane Joaquin (Fig. 2.6a-c), and they were nearly perpendicular for all three flights. However, on 5 Oct 2015, Hurricane Joaquin was far enough from the US coast that only one radial pass was able to be flown into Hurricane Joaquin's inner core (Fig. 2.6d).

Since 2 Oct 2015 was the first flight into a major hurricane that utilized the HDSS dropsondes, the rapid-fire portion of the flight was shorter than the subsequent days. Thus, fewer dropsondes were deployed for this analysis. However, due to the general success of that flight and the uncertainty of having another favorably-located TC to sample, the rapid-fire portions were lengthened in Hurricane Joaquin and more sondes were released on subsequent days.

Fig. 2.7 shows that the axisymmetric inner core coverage is well sampled. However, the conservative flight on 2 Oct 2015 showed that there is a large gap in data coverage from approximately $90-130$ km (Fig. 2.7a). 3 Oct 2015 had the best sampling of the analyzed v_{max}, (Fig. 2.7b), and 4 Oct 2015 has the best axisymmetric data coverage (Fig. 2.7c).While 5 Oct 2015 only had one radial pass, it also has very good coverage across the domain (Fig. 2.7d).

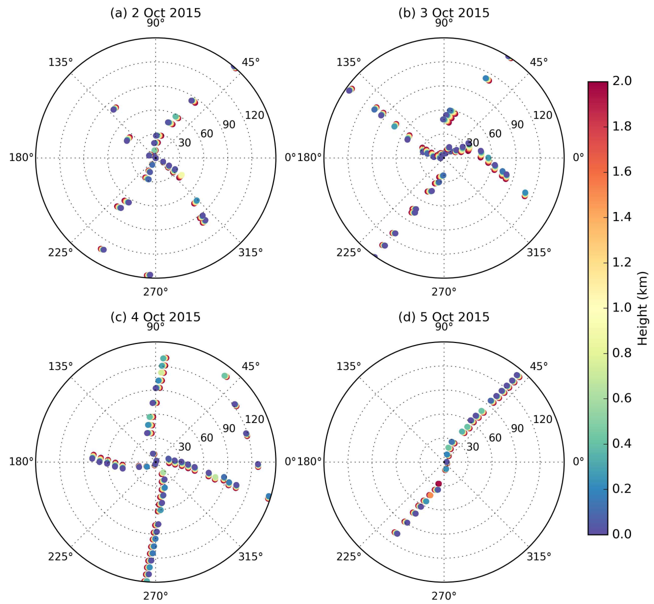

FIG. 2.6. Storm-motion adjusted azimuthal locations of dropsondes for Hurricane Joaquin from 2 – 5 Oct 2015. Shading denotes the height of the individual dropsonde data points from 2 km to the surface.

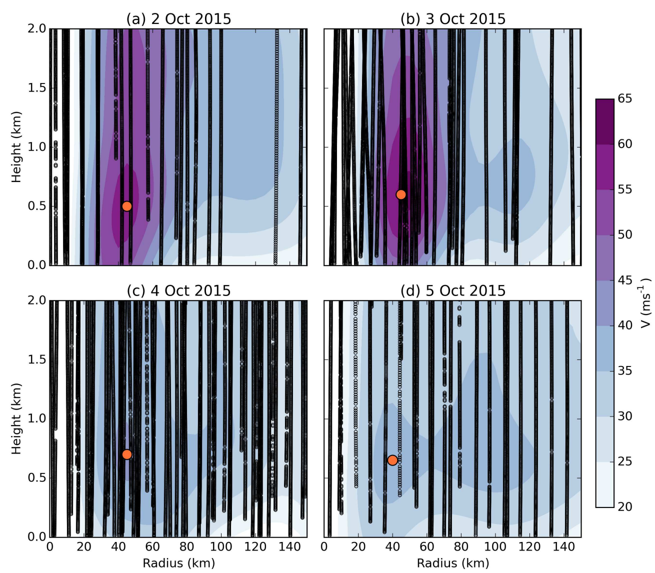

FIG. 2.7. Black scatter points show the axisymmetric radius-height dropsonde data locations for Hurricane Joaquin from 2 – 5 Oct 2015. Shading denotes the SAMURAI-analyzed axisymmetric tangential wind speed for reference, and the orange scatter points denote the specific maximum tangential wind location for reference.

However, while 5 Oct 2015 had a slightly larger v_{max} around 90 km, the maximum analyzed in this study was constrained to be located in the inner local maximum to stay more consistent with the previous days. Regardless, retrieval results are quite similar for both maxima.

CHAPTER 3

Results

3.1 Experiment 1: the Control Experiment

Experiment 1 is regarded as the control experiment, in which all the default settings of the axisymmetric version of CM1 are used. Fig. 3.1 shows the time series of $ILPI$, the maximum tangential wind component, the radial wind component at that location, the radius and height of the maximum tangential wind, and both the CM1 drag coefficient and the retrieved drag coefficient calculated from Eq. 2.16 for 1-hour output. The TC becomes quasi-steady around 90 hr into the simulation, although "quasi-steady" still entails fluctuations of v_{max} greater than 10 m s^{-1} about the running mean (Fig. 3.1a). However, despite the large v_{max} fluctuations involved, there is no apparent bias in retrieved $ILPI$ or the Integral Form of C_D when using Eqs. 2.13 and 2.16, respectively, and the means of both time series appear to be centered close to their respective prescribed "truth" values. In addition, $ILPI$ is able to increase with v_{max} during the intensification period and plateau during the quasi-steady steady period just from TCBL structural parameters, such that there is also not a clear bias difference in either $ILPI$ between the intensifying and quasi-steady portions of the simulation.

However, note that the $ILPI$ and C_D derivations are not valid when there is radial outflow located at v_{max} because they become negative in those instances, which is primarily due to artifacts of the model level discretization (Fig. 3.1c). In fact, retrievals show that there is a large sensitivity to u_m, since the time series fluctuations for both $ILPI$ and C_D closely resemble the negative of the u_m time series. The most clear example of this is that $ILPI$ becomes negative when $u_m > 0$ m s^{-1} during the transition from intensifying to quasi-steady, which is expected from Eq. 2.13 because u_m is the only term that can realistically change sign in a TC. Furthermore, since most $ILPI$ local minimums tend to be collocated with v_{max} local minimums, this suggests that $ILPI$ is a diagnostic parameter, rather than a prognostic one.

In addition to u_m, Fig. 3.1b shows that r_m is consistently and gradually increasing over time for the duration of this simulation. In contrast, after the TC becomes quasi-steady, z_m appears to fluctuate around 1 km instead of continuing to increase like the radius, and z_m is noisier and fluctuates more than r_m does. Thus, even though the TC is gradually expanding in size with increasing time, the TCBL depth is relatively constant. Furthermore, when comparing z_m with u_m, there appears to be a greater likelihood

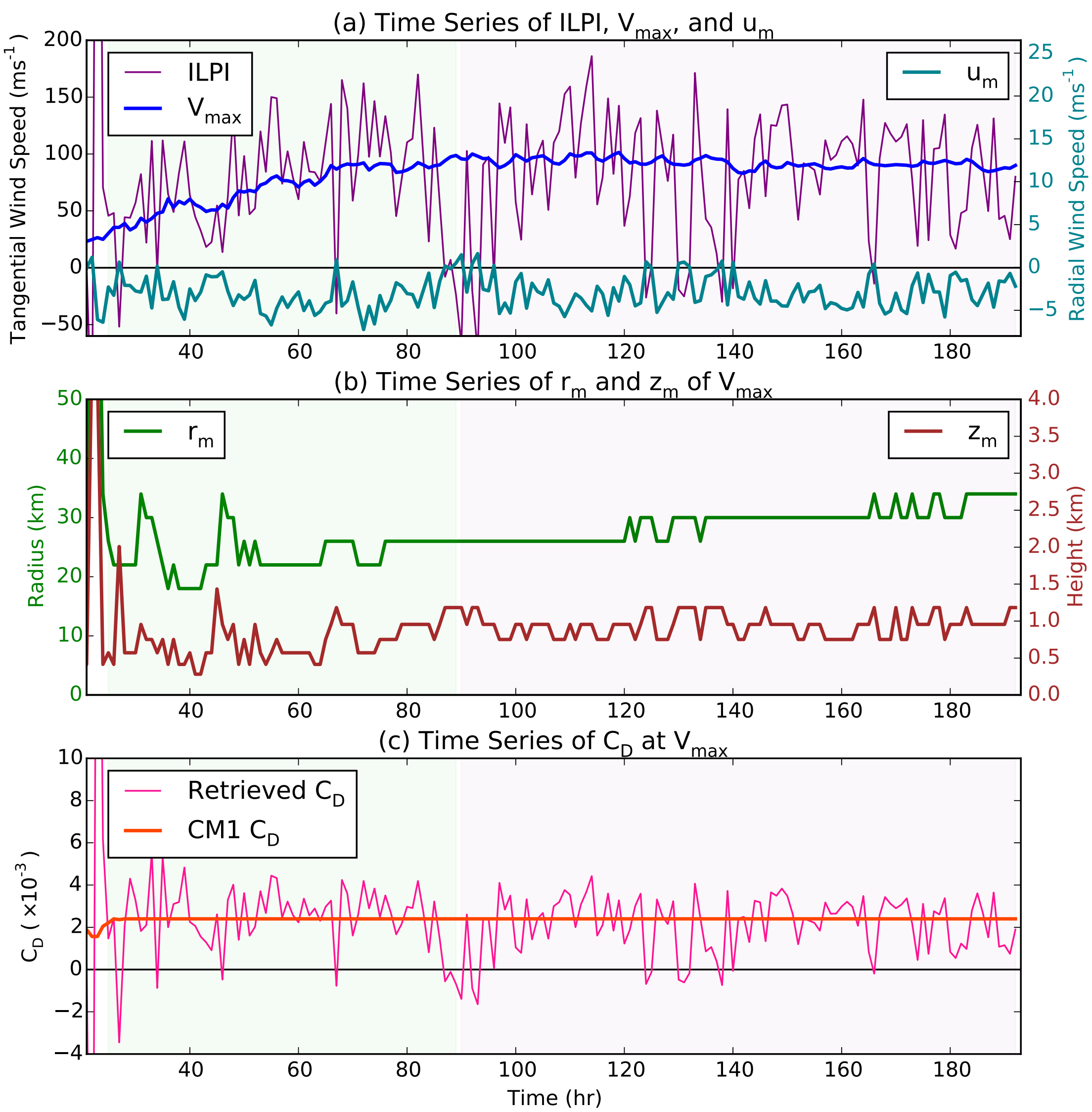

FIG. 3.1. Time series of (a) $ILPI$ from Eq. 2.13 (purple), v_{max} (blue), and the radial wind located at v_{max} (u_m; teal) in m s^{-1}; (b) z_m (brown) and r_m (green) in km; and (c) CM1 C_D (orange) and retrieved C_D (pink). The radial wind u_m is plotted using the second y-axis in (a), which is aligned such that 0 m s^{-1} is in the same position for both axes. Shading denotes approximate times when the TC is intensifying (mint), and quasi-steady (lavender). Bold lines denote CM1 values, and thin lines represent retrieved values.

of u_m becoming positive when z_m is larger, and this relationship between u_m and z_m will be further explored in Experiment 2.

Since the default CM1 C_D quickly becomes capped at a constant $C_D = 2.4$ at r_m after the TC has spun up, C_D can be set constant for additional testing. Therefore, to test a greater number of C_D values, C_D will be set constant at the values previously discussed in Section 2.2 for the next experiment.

3.2 Experiment 2: Varying C_D

Experiment 2 keeps C_D and C_K constant and equal to each other to test a larger number of drag coefficients. While this experimental setup is different from Smith et al. (2014) in that they used a different three-dimensional model and kept C_K constant across all simulations, the results of Experiment 2 are qualitatively similar to their results before approximately $t = 80$ hr (Fig. 3.2). In particular, the intensification rates dramatically increase until C_D is approximately equal to the default maximum value of Experiment 1, and then the intensification rates have minimal differences above $C_D = 2.5$. Interestingly, while Montgomery et al. (2010) and Smith et al. (2014) speculated that axisymmetric models cannot produce the same intensification results as a three-dimensional model when C_D is modified, the similarity of results between this axisymmetric study and the three-dimensional studies of Montgomery et al. (2010) and Smith et al. (2014) suggest otherwise.

However, after approximately $t = 80$ hr, there is a "sorting effect," in which the simulation with the highest $C_D = 4.5$ has the lowest quasi-steady v_{max}, and it steadily increases as C_D is reduced until the lowest $C_D = 1.0$ has the highest quasi-steady v_{max} (Fig. 3.2). In other words, after approximately $t = 80$ hr, Experiment 2 more closely resembles the results of Emanuel (1995), and this result is shown more clearly in Fig. 3.3. Therefore, the transitioning behavior of v_{max} with respect to C_D corroborates that some of the conflicting results discussed in Section 1 are simply due to differences in simulation time lengths (Bryan 2013), and that the C_D aspect of traditional MPI theory is not applicable to TCs that have yet to reach MPI.

In addition to showing the monotonic decrease of the quasi-steady v_{max}, Fig. 3.3 also shows that the height of v_{max} increases with increasing C_D, and the radius of v_{max} shows slight evidence of decreasing with increasing C_D. However, the relatively coarse radial resolution of 4 km partially obscures this relationship. Additionally, the maximum near-surface inflow increases from slightly over 30 m s^{-1} to over 33 m s^{-1}, and while not clear in Fig. 3.3, the 10-m tangential wind speed also decreases with increasing C_D. These results are consistent with an increased agradient torque as C_D is increased, as Smith et al. (2014) discuss. In addition, these relationships are also qualitatively consistent with Eq. 2.16.

In addition to the 6-hour average of the quasi-steady TC, the behavior of the remaining variables besides v_{max} in $ILPI$ and both C_D retrievals can also be directly examined for the duration of the Experiment 2 simulations after model spin-up. The general time series for u_m, r_m, and z_m are qualitatively similar to Fig. 3.1 (not shown), but systematic changes in magnitude are apparent in both the means and the spread of the variables as the specified C_D in CM1 is increased (Fig. 3.4). In terms of spread, u_m

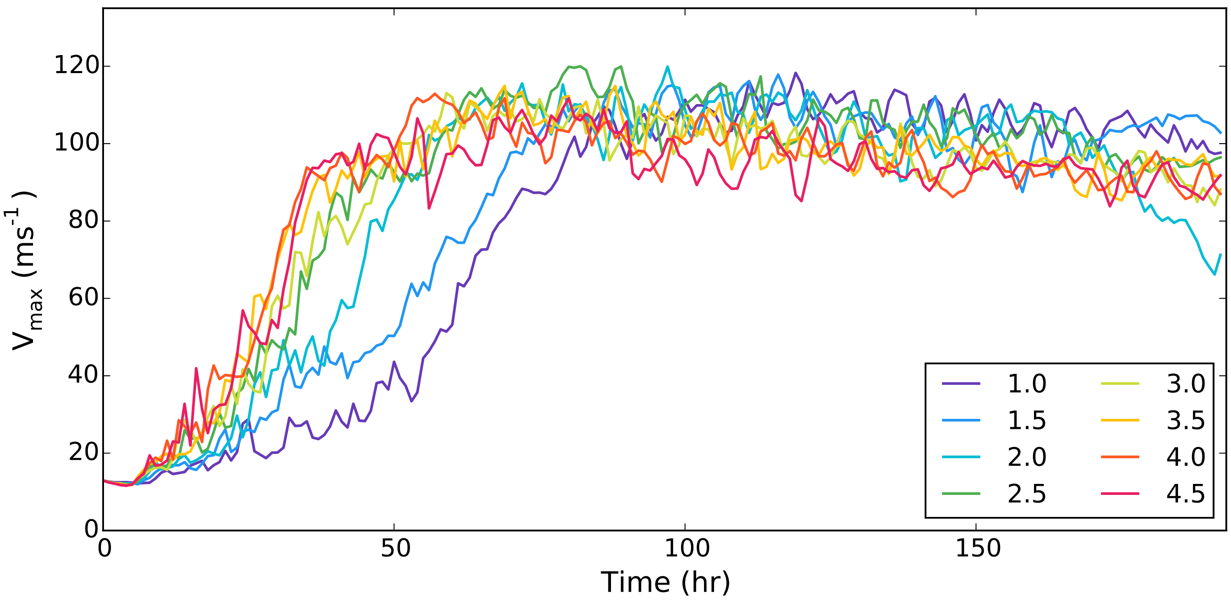

FIG. 3.2. Time series of v_{max} for 8 CM1 simulations where C_D is held constant and ranging from $C_D = 1 - 4.5$. Colors for each simulation are kept consistent throughout this study.

transitions from almost exclusively negative, inflow values to more frequent instances of positive, outflow values, and the means of u_m become less negative as C_D is increased in CM1 (Fig. 3.4a). The more frequent positive u_m values are likely an artifact of the discrete vertical model levels trying to capture the increasing gradient of radial wind as C_D is increased.

The weakening of inflow at v_{max} is associated with an increase in the height of v_{max}, such that the mean z_m height after model spin-up transitions from approximately 0.6 km to approximately 1.2 km (Fig. 3.4b). Since the height of v_{max} is regarded as near the top of the TCBL in this study, this increase in height means that the TCBL depth approximately doubles when C_D is increased from 1.0 to 4.5 in these axisymmetric CM1 simulations.

Corresponding with this increase in TCBL depth, α^2 strongly decreases as C_D is increased, and it has relatively little spread for each simulation (Fig. 3.4c). Physically, the decrease in α^2 means that the difference between v_{max} and v_{10} is becoming larger as C_D is increased. Since the quasi-steady v_{max} decreases slightly as C_D is increased (Fig. 3.2), the decrease in α^2 is largely a result of v_{10} more drastically decreasing as C_D is increased (not shown). The larger decrease in v_{10} is expected because a larger C_D implies increased surface friction, and larger surface friction leads to a larger near-surface agradient torque that leads to a larger radial wind component at the expense of the 10-m tangential wind component.

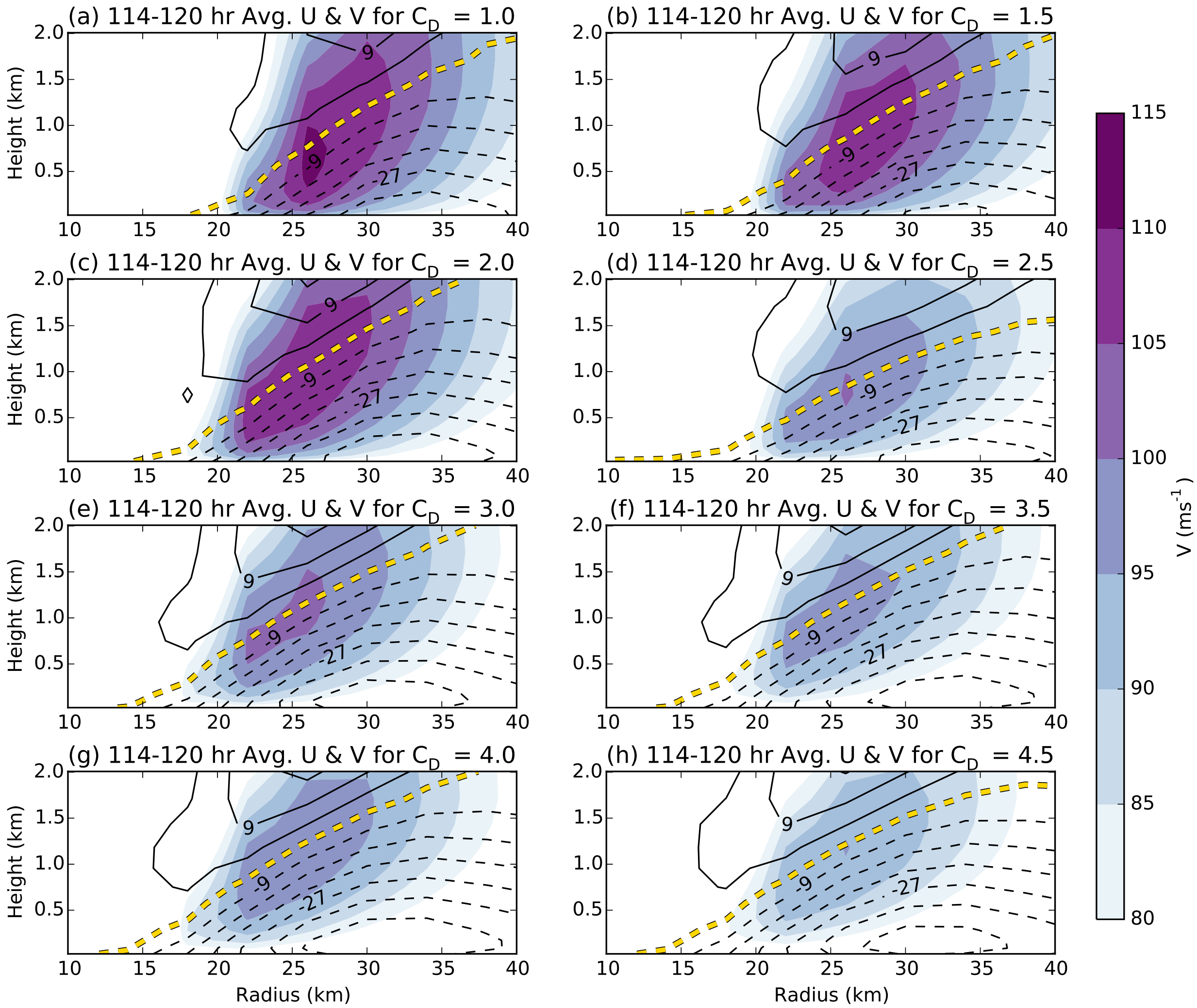

FIG. 3.3. Radius-height cross-sections of the 8 axisymmetric CM1 simulations averaged from 114-120 hr as in Smith et al. (2014). Shading denotes the averaged tangential wind, where shading starts at 80 m s^{-1} to highlight the maximum wind speeds. Contours denote the averaged radial wind, where the contours are every 6 m s^{-1}. The -3 m s^{-1} radial wind contour is highlighted in gold for emphasis.

The radius of v_{max}, r_m, also shows slight evidence of decreasing with increasing C_D, but this relationship is much less pronounced than the others (Fig. 3.4d). The means of the simulations generally slightly decrease, except for the $C_D = 4.5$ simulation. Given that the radial grid spacing is 4 km in this study, the last few Experiment 2 simulations may need a smaller grid spacing to adequately resolve smaller r_m. However, the spread of r_m values across the simulations still exhibit the general trend of r_m decreasing with increasing C_D. In addition, while the largest r_m values for $C_D = 1.0 - 1.5$ are associated with the TC still intensifying to maximum intensity, the general decreasing r_m trend as C_D is increased still holds when only including the points that occur after the maximum intensity of each simulation. However,

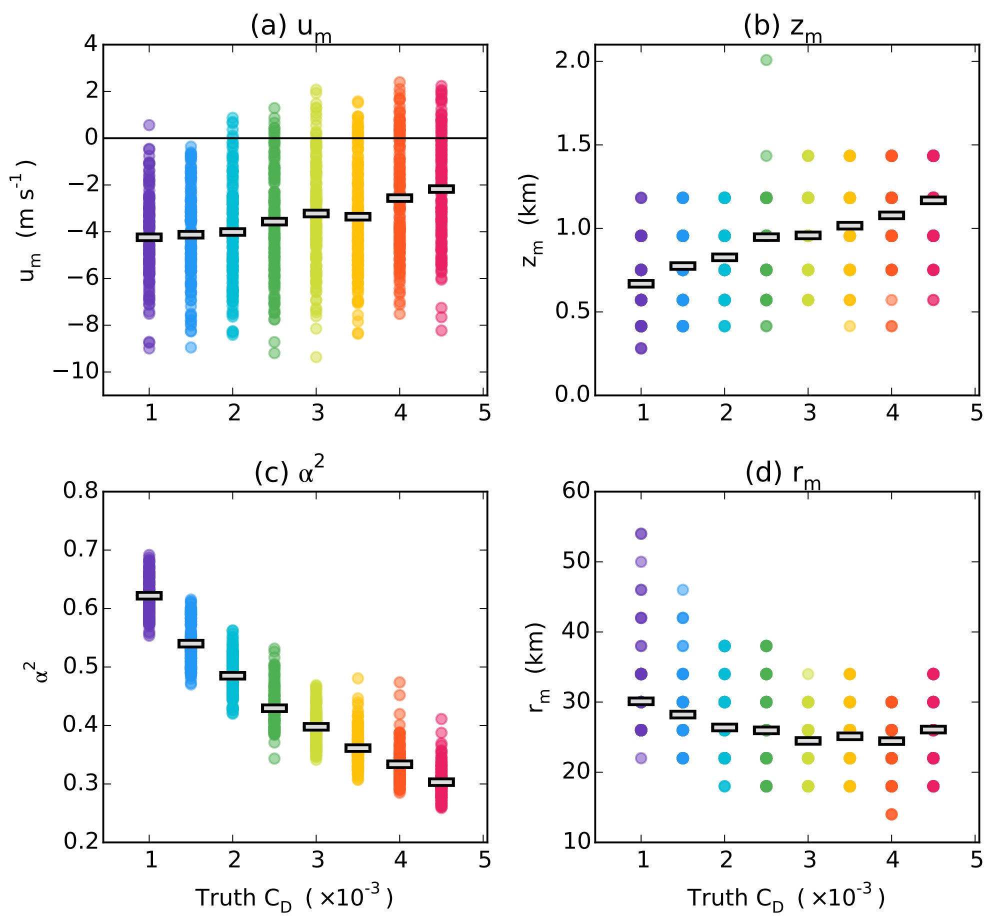

FIG. 3.4. Values of: (a) radial inflow at the location of v_{max} (u_m; m s-1); (b) height of v_{max} (z_m; km); (c) $\alpha^2 = (v_{10}/v_{max})^2$; and (d) radius of v_{max} (r_m; km) after $t = 48$ hr. Black and gray rectangles denote the mean of the values for each simulation after $t = 48$ hr.

the primary difference is that the mean r_m decreases by about $3-5$ km when stratifying the data in this manner (not shown).

Overall, Figs. 3.2–3.4 indicate that the newly-derived relationships of the variables in Eq. 2.18 with respect to C_D are qualitatively consistent with the structural changes of the axisymmetric CM1-modeled TCBL in response to changes in the magnitude of C_D. Therefore, the quantitative reasonableness of the newly derived relationships will be explored in the following sections.

3.2.1 Integral Form

Before assessing the skill of the C_D retrievals, the $ILPI$ from Eq. 2.13 is explored first. When comparing with the $ILPI$ retrieved in Experiment 1, results show that the Experiment 2 $ILPI$ are noisier when C_D is held constant than when it is allowed to vary with wind speed (Figs. 3.1a, 3.5). In addition, there is a systematic bias in $ILPI$ that is dependent on the prescribed C_D in CM1. For lower magnitudes of

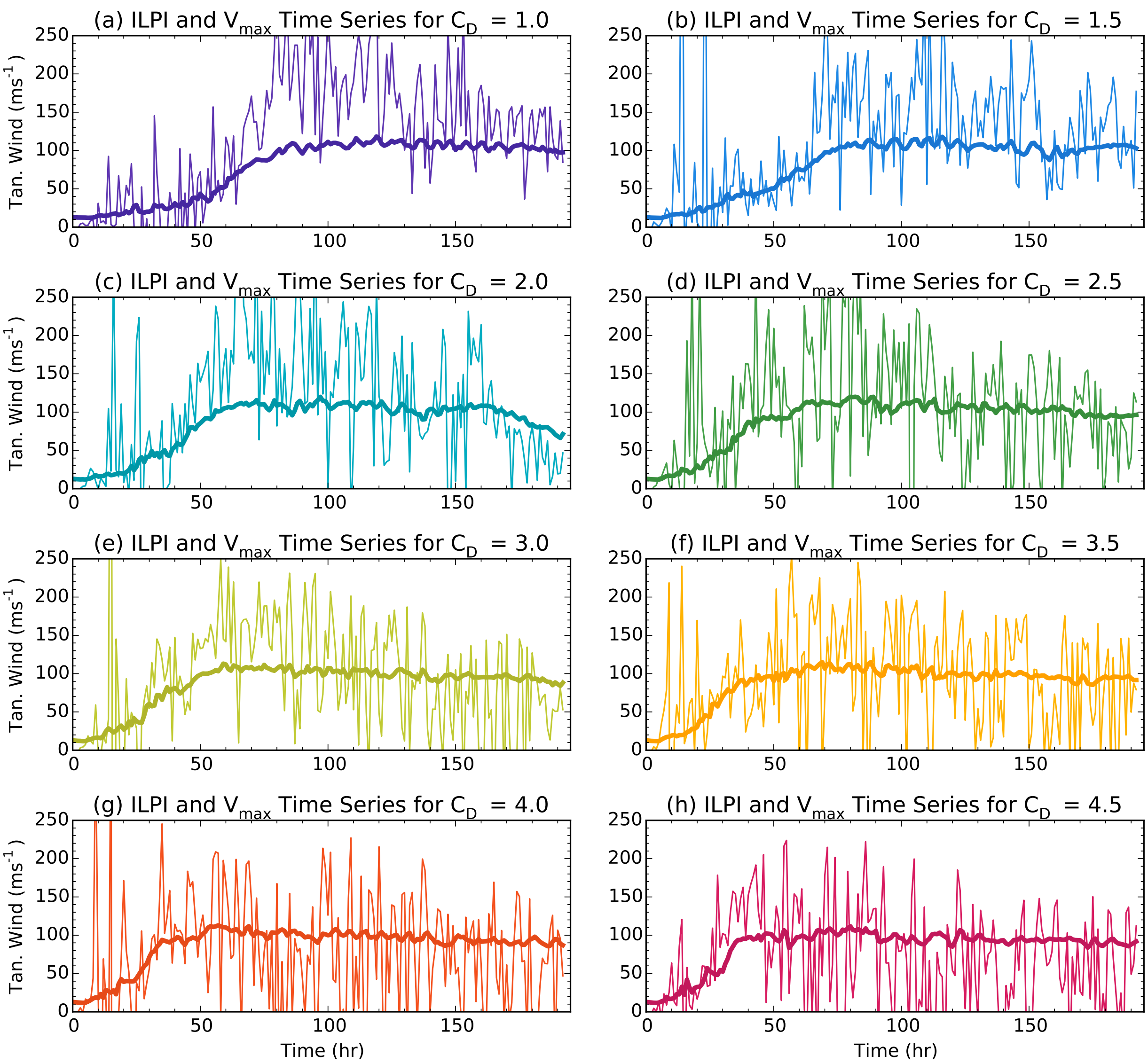

FIG. 3.5. $ILPI$ (thin) and v_{max} (thick) time series for constant C_D ranging from 1 - 4.5.

prescribed C_D, there is a substantial high bias in $ILPI$ when v_{max} becomes quasi-steady. However, the bias decreases as C_D increases, such that there is a minimal bias when $C_D \approx 2.5$, and a clear low bias when $C_D = 4.5$.

Interestingly, while $C_D = 2$ exhibits a high $ILPI$ bias before $t = 150$ hr, it shifts to a low bias shortly afterwards, which is accompanied by a corresponding decrease in v_{max}. Since the shift in v_{max} is captured by the $ILPI$ parameters in Eq. 2.13, this suggests that this decrease in maximum intensity is due to changes in TCBL structure.

In addition to examining $ILPI$, the Integral Form of C_D retrievals in Eq. 2.16 can also be examined, and it exhibits similar patterns to $ILPI$ (Fig. 3.6). For the lowest prescribed CM1 C_D, there is a high bias

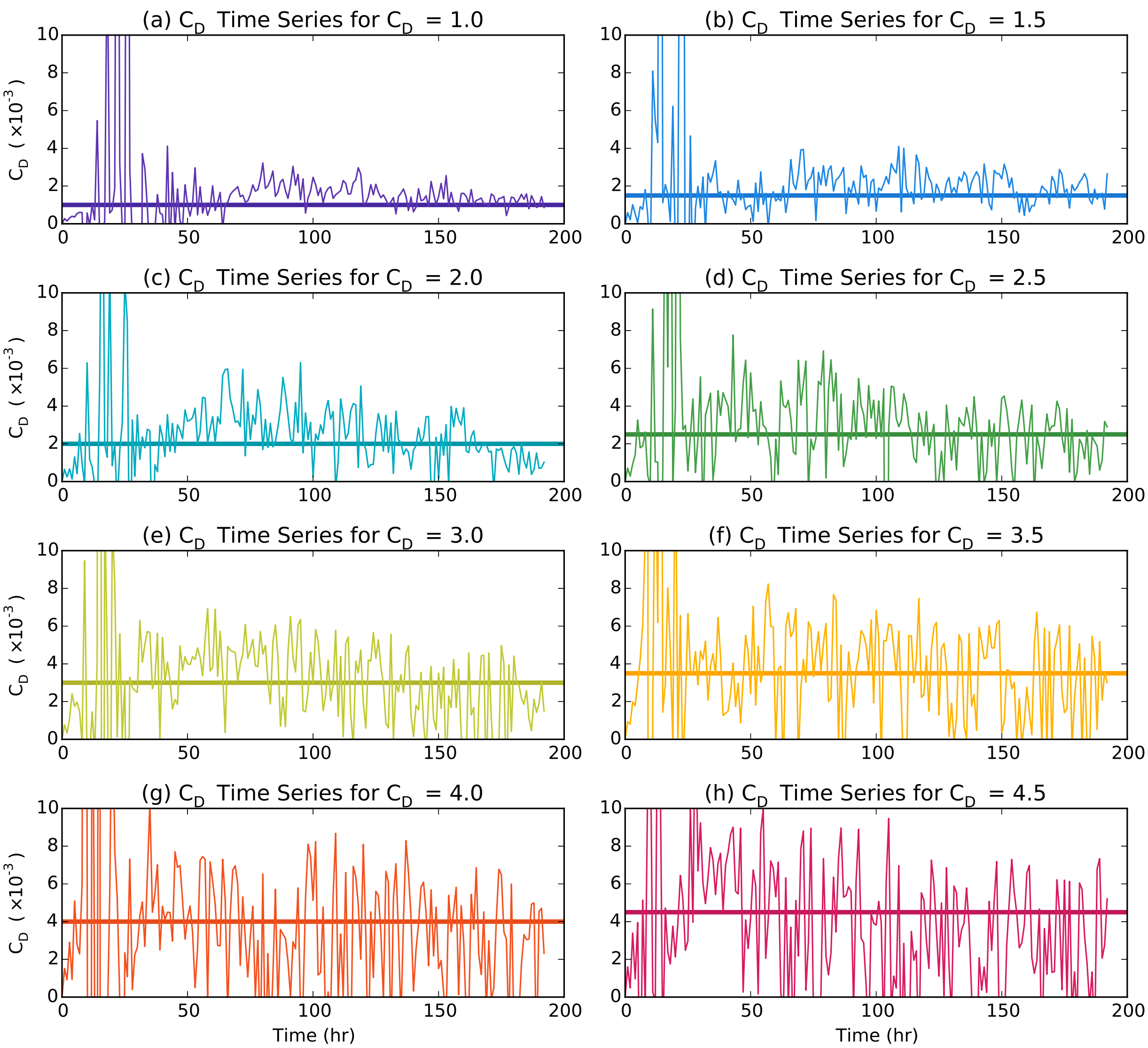

FIG. 3.6. Integrated Form time series of retrieved C_D (thin) and CM1 "truth" C_D (thick).

in retrievals, which steadily shifts to a low bias for the highest prescribed C_D values. However, one result that is more obvious with C_D than with $ILPI$ retrievals is that the magnitude of the noise is proportional to the value of the prescribed CM1 C_D; as C_D increases, so does the noise in the retrievals. Nevertheless, the approximate mean also increases; thus Eq. 2.16 is capturing a physical response in TCBL structure from changes to C_D.

The variability in the Integral Form of C_D retrievals can be more quantitatively assessed through the normalized distributions of its residuals for each simulation (Fig. 3.7). The distributions show that as C_D is increased to higher values, they become less peaked. Standard deviations also show that they are less than 200% of the CM1 C_D, except for the $C_D = 2.5$ simulation that has a large outlier skewing

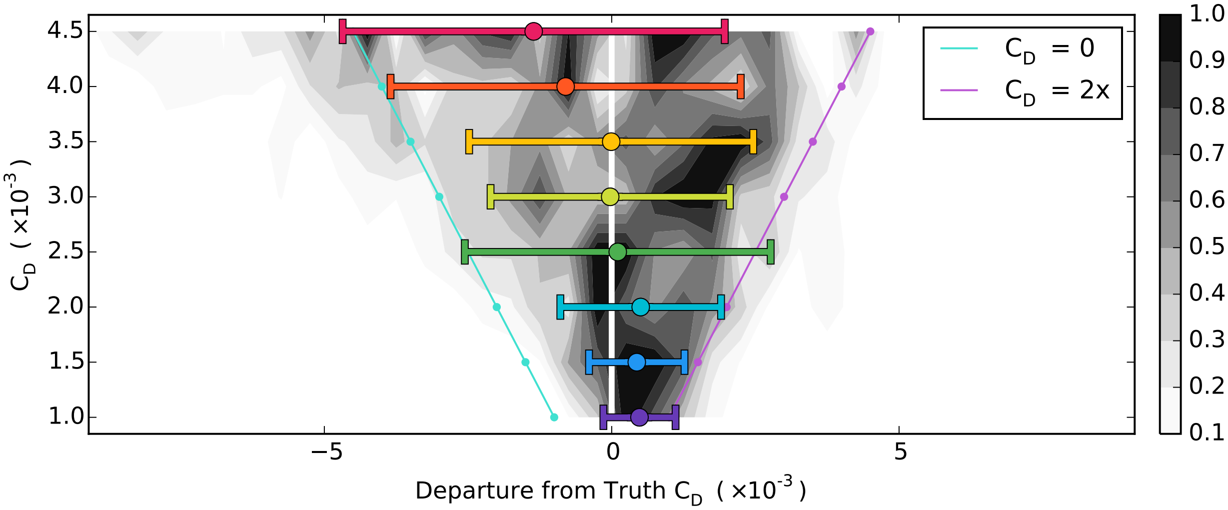

FIG. 3.7. Normalized, stacked histograms with a bin width of 0.5 (shading), means (scatter points), and standard deviation (error bars) of C_D residuals for each simulation. Turquoise line denotes the line where $C_D = 0$, and the light purple line denotes where C_D is twice the set CM1 "truth" value.

the distribution. In addition, the averages of the distribution confirm that the retrieval biases become lower than the CM1 C_D as CM1 C_D is increased. Furthermore, there are also more frequent instances of negative C_D retrievals as the prescribed C_D is increased above $C_D = 2.5$.

Overall, while there is considerable spread in C_D retrievals, the Integral Form shows some skill in retrieving C_D from TCBL structure in the sense that the mean of each simulation is close to the prescribed truth C_D. However, the time tendency term is difficult to interpret, and its necessity for C_D retrievals will be scrutinized in the next section.

3.2.2 Differential Form

To assess the necessity of the time-tendency term in the Integral Form of C_D retrievals, the results of the Differential Form of C_D retrievals in Eq. 2.18 will be compared with the previous results. When comparing Fig. 3.6 with Fig. 3.8, the two time series are nearly identical, aside from a few retrievals during the model spin-up time when the TCBL structure is rapidly changing. Since the Differential Form of C_D retrievals does not include a time-tendency term but provides nearly identical results to the Integral Form, this means that the time-tendency term in the Integral Form is generally close to 1, and that it can be neglected. Thus, the Differential Form of C_D retrievals will be used for the rest of this study due to its simplicity.

Fig. 3.9 shows the magnitude of C_D specified in CM1 versus the magnitude of the Differential Form of C_D. It also shows the line at which the two magnitudes are equal, such that points above the line are a

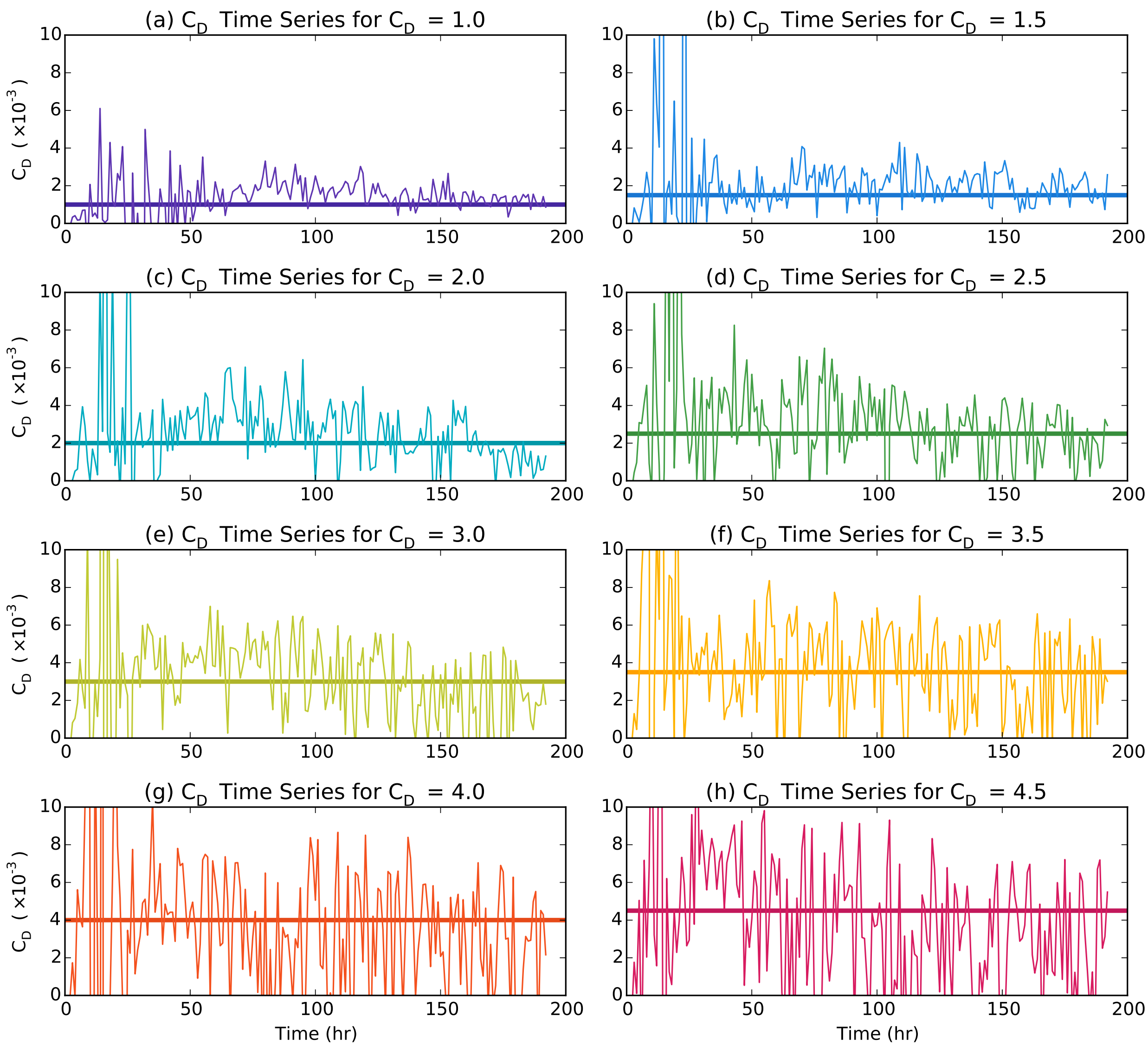

FIG. 3.8. As in Fig. 3.6, but for the Differential Form of C_D retrievals (Eq. 2.18).

retrieval overestimate, and vice versa. When the Differential Form C_D magnitudes are directly compared to their prescribed CM1 C_D magnitudes, results again show that the spread is increasing as CM1 C_D is increased (Fig. 3.9). In addition, there are more frequent instances of unphysical, negative C_D retrievals as the CM1 C_D is increased, which correspond with v_{max} being located at higher heights (Fig. 3.9a). Interestingly, α^2 appears to be roughly constant for an individual simulation, but there is monotonic decrease in the specific value of it as the CM1 C_D is increased (Fig. 3.9b). Since z_m and α^2 both increase with increasing C_D, there is a likely direct relationship between the two. In addition, when the two variables are divided as in Eq. 2.18, results show that the pattern more closely resembles z_m, since z_m has larger variability within an individual simulation (Fig. 3.9c).

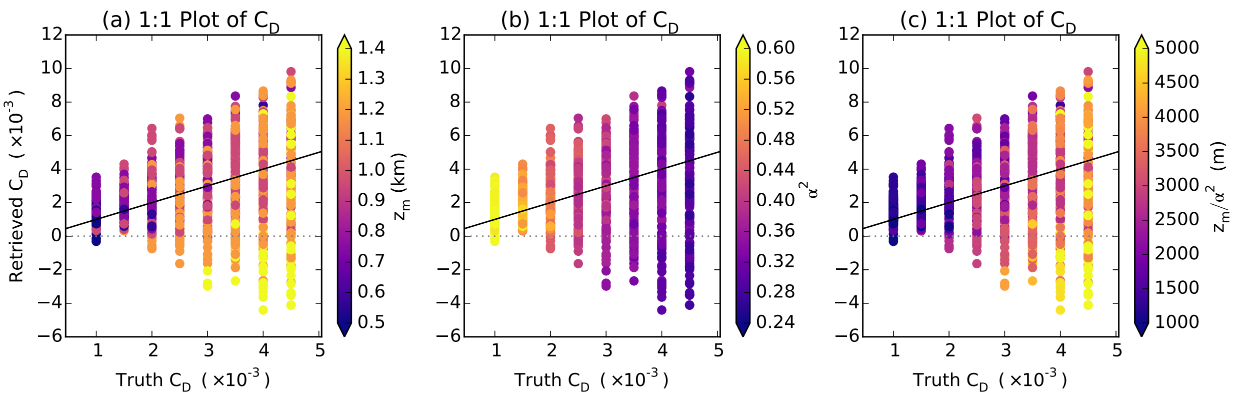

FIG. 3.9. One to one plot of CM1 "truth" C_D vs. Differential Form C_D. Black line denotes where the two values are equal. Shading denotes: (a) the height of v_{max} (z_m; km); (b) the vertical scaling factor (α^2); and (c) the ratio between the two (m).

In contrast to the direct relationship of z_m and α^2, closer examination of r_m and v_{max} shows that they instead appear to have an inverse relationship—where larger magnitudes of v_{max} appear to correspond with smaller magnitudes of r_m (Fig. 3.10a-b). This inverse relationship makes sense because the two variables become relative angular momentum (RAM) when multiplied together. While RAM is not conserved in the TCBL, Fig. 3.10 seems to suggest that RAM in the TCBL tends to decrease as C_D is increased, because the highest overall RAM (lowest inverse RAM) appears to be found in the simulations with the lowest CM1 C_D, and the largest values of RAM in each simulation tend to decrease with increasing C_D. For example, the $C_D = 1$ simulation has the most instances of RAM > 3,500 m^2 s^{-1}, and $C_D = 4.5$ only has a few instances of RAM > 3,000 m^2 s^{-1}. In addition, it appears that the points with the lowest RAM (highest inverse) have the highest bias with respect to the 1:1 line (Fig. 3.10c), which suggests that RAM is more sensitive to changes in r_m than v_{max} when comparing with the corresponding points in Fig. 3.10a-b.

However, when examining u_m, a surprising result emerges; C_D retrievals which have $u_m \approx -3$ m s^{-1} have the smallest error, regardless of the prescribed C_D value (Fig. 3.11). Fig. 3.11b shows the normalized residuals of the retrievals, where the residuals are the retrieved C_D minus the CM1 C_D, and they are then normalized by the CM1 C_D. This means that positive percentages are retrievals that are higher than the CM1 C_D, and vice versa. Since Zhang et al. (2011) show that u_m scales as approximately 25% of the peak radial inflow, a small inflow magnitude at the location of v_{max} was expected. However, an "optimal" inflow magnitude of -3 m s^{-1} for every tested C_D was not expected, especially since the range of magnitudes of the normalized $u_m = 25\%$ results of Zhang et al. (2011) is approximately $-6.4 < u_m <$

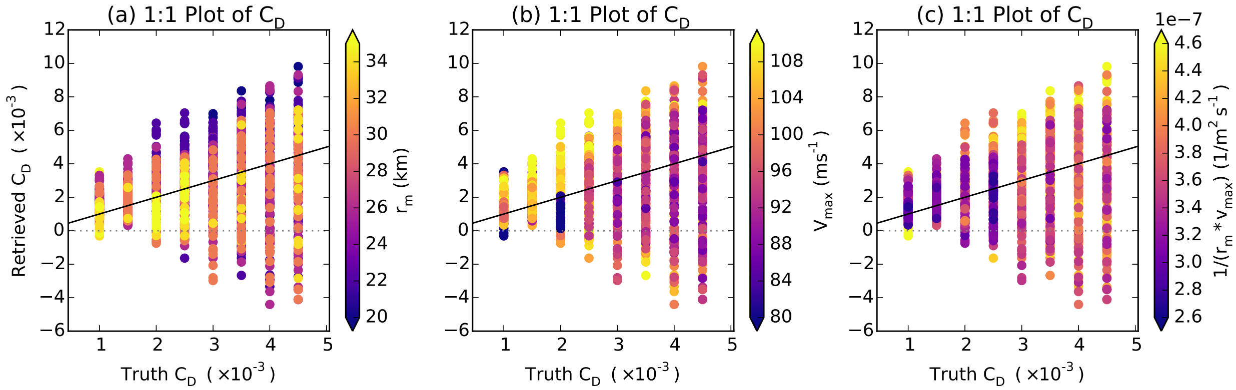

FIG. 3.10. As in Fig. 3.9, but shading denotes the magnitude of: (a) r_m (km); (b) v_{max} (m s^{-1}); and (c) the inverse of the product of the two $\left(1/\text{m}^2\ \text{s}^{-1}\right)$.

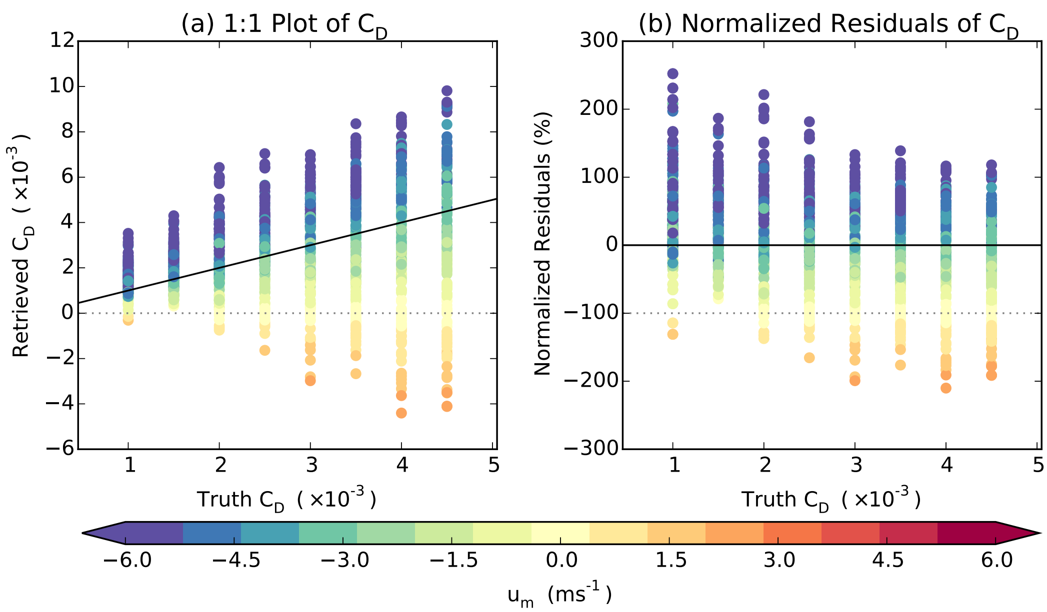

FIG. 3.11. (a) As in Fig. 3.9, but shading denotes u_m (m s^{-1}). (b) Normalized residuals of the Differential Form retrieved C_D shaded as in (a), and -100% is equivalent to $C_D = 0$.

-5 m s^{-1}. In contrast, the average CM1 u_m magnitudes in this study range from -4.3 m s^{-1} to -2.2 m s^{-1} as C_D is increased, and the spread of individual u_m values ranges from -9 m s^{-1} to nearly 3 m s^{-1} (Fig. 3.4a). Thus, while the results of Zhang et al. (2011) are more negative than this study's average u_m, they are within the range of the modeled values in this study.

In addition to highlighting the $u_m = -3$ m s^{-1} relationship along the 0-residual line, the retrievals can be binned by different time lengths and then averaged, and the normalized residuals of these time-averaged retrievals can be examined (Fig. 3.12). Results show that the normalized residuals steadily

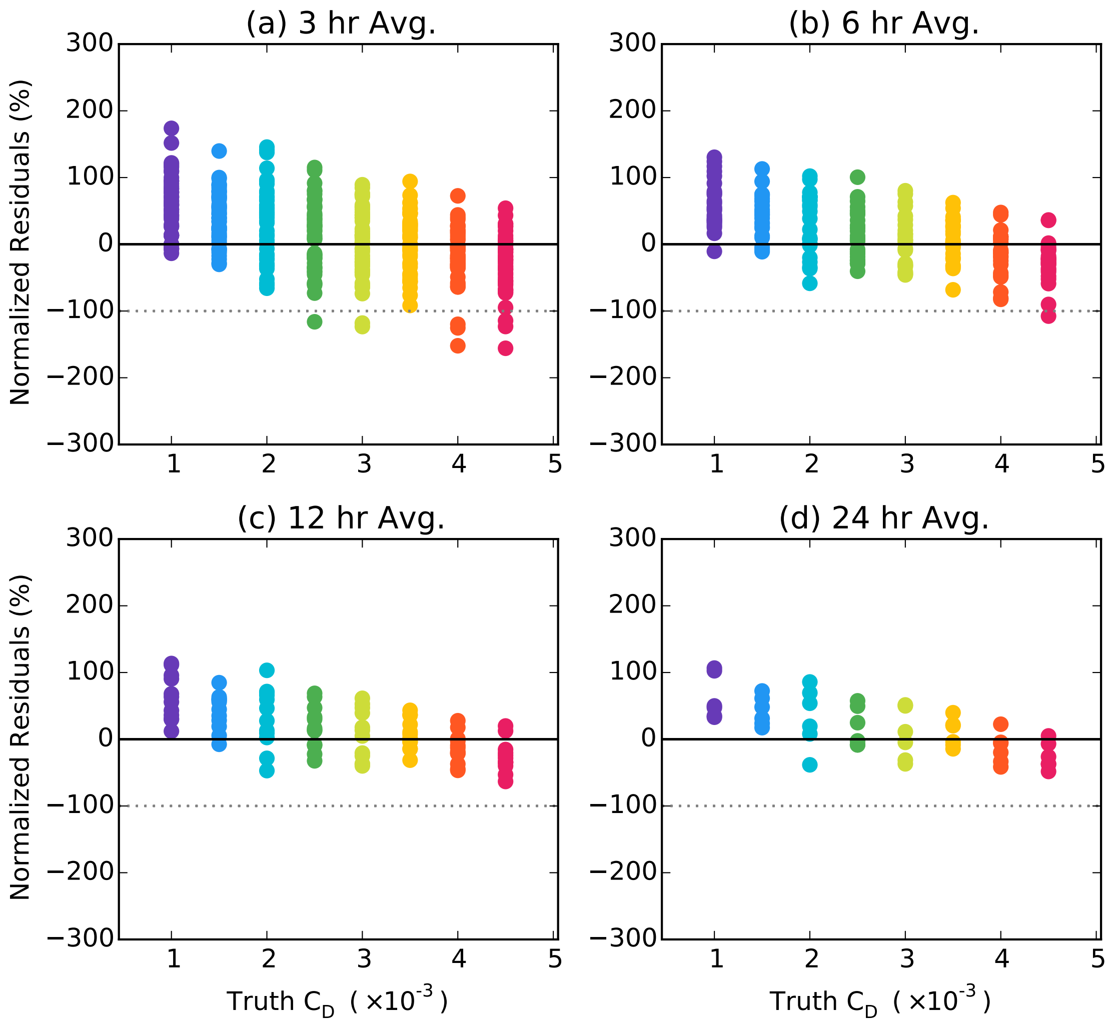

FIG. 3.12. Normalized residuals of Fig. 3.8 when averaging output for: (a) 3 hr bins, (b) 6 hr bins, (c) 12 hr bins, and (d) 24 hr bins. Results exclude the first 48 hours of initial model spin-up. The dotted line at -100% shows where $C_D = 0$ for reference.

reduce to within 100% of the CM1 C_D when averaged over 24-hr bins (Fig. 3.12d), which suggests that the Differential Form performs better in a time-averaged structure sense, rather than instantaneously. Thus, while the TCBL structure is continually fluctuating and is not in a strict balanced state, the Differential Form can provide insight into the TCBL time-mean structure.

However, while the noise in retrievals is appreciably reduced when averaged over increasing lengths of time, there is still a negative linear trend remaining as C_D is increased (Fig. 3.12). This linear trend is due to some temporal characteristics over the simulations (not shown). The highest biases in each simulation tend to occur just as the TC is becoming quasi steady, and the Differential Form tends to overshoot the transition from the intensifying regime to the quasi-steady regime. The lowest biases tend to occur at the ends of the simulations, although the Differential Form retrievals for $C_D = 1.0 - 1.5$ have slight high biases throughout the entire simulations.

Another interesting result is that even though outflow at v_{max} is the only way to make $ILPI$ and C_D retrievals become negative, it is not correlated with hourly $\partial v_{max}/\partial t$ (not shown). While this result could have been attributed to the hourly time step not properly resolving all of the TC intensity fluctuations, 1-minute output of $\partial v_{max}/\partial t$ output was also examined, and there was still no correlation (not shown). While this result is initially unintuitive, a likely reason for the lack of correlation between u_m and $\partial v_{max}/\partial t$ is because the location of v_{max} is frequently changing. Thus, while the radial inflow structure may not be changing much, the inflow at v_{max} would be changing as the location of v_{max} changes. This change in v_{max} location occurs vertically more frequently than radially, which partially explains the more frequent fluctuations in z_m than in r_m that were seen in Experiment 1. Since the gradient of inflow is also much larger in the vertical than the horizontal, the periodic shifts in v_{max} height would account for a large portion of inflow variability.

When looking more closely at the relationship between u_m and normalized residuals, results show that while there is a range of inflow values that result in minimal error, there is an apparent linear trend with a 0-residual intercept at approximately -3 m s^{-1} for nearly every simulation (Fig. 3.13). However, the linear trend is also heteroskedastic with increasing spread as u_m becomes increasingly negative, which suggests that the other terms—r_m, z_m, v_{max}, and α^2—have increasing influence on retrievals as inflow increases. The primary reason for this heteroskedasticity is that $u_m = 0$ m s^{-1} forces $C_D = 0$, which means that the other terms can only have a minimal effect on retrievals when $u_m \approx 0$ m s^{-1}.

Since $u_m = -3$ m s^{-1} is associated with the least amount of error, the next section seeks to quantify the increase in retrieval skill if the assumption $u_m = -3$ m s^{-1} can be made.

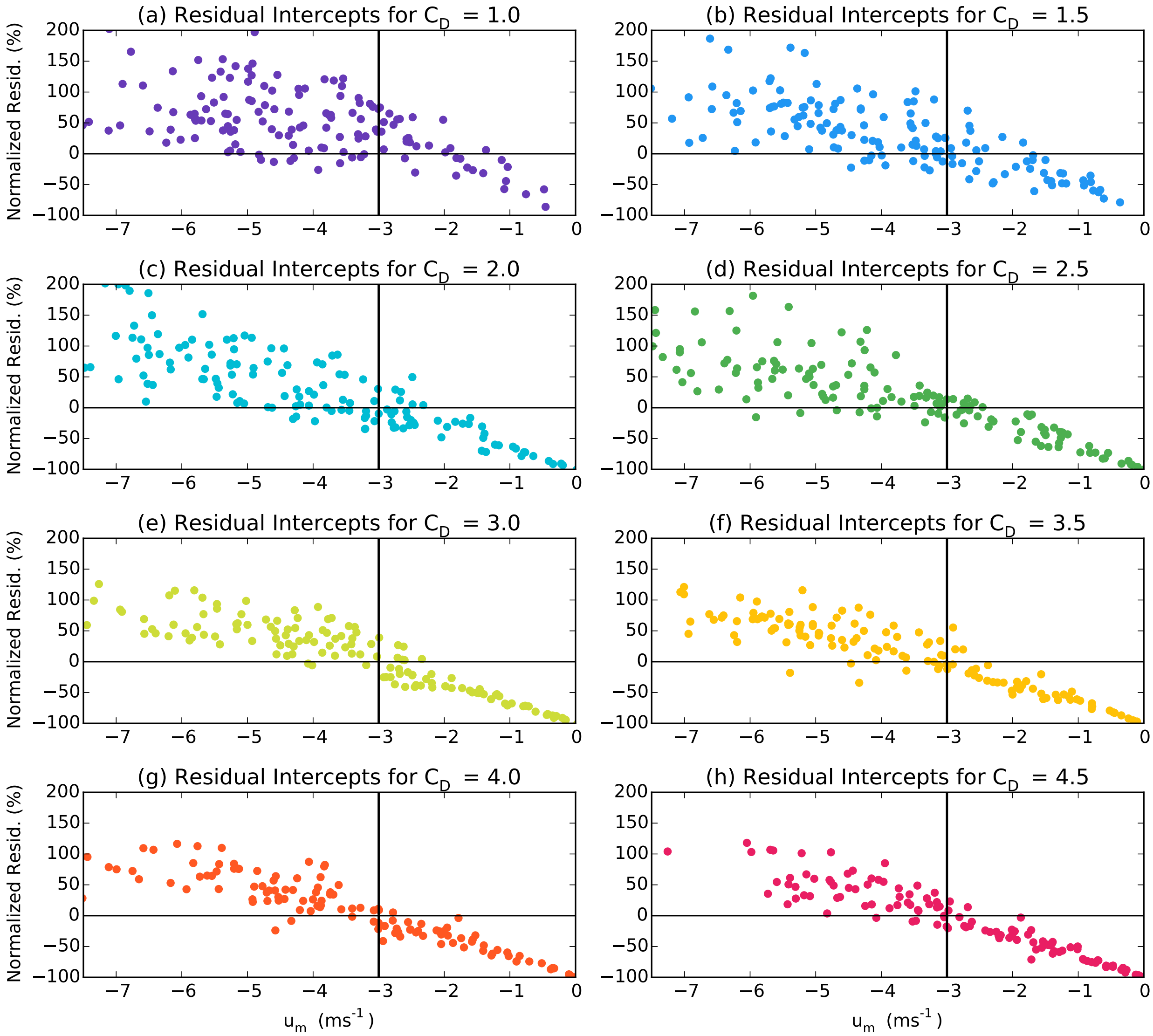

FIG. 3.13. Relationship between u_m and normalized residuals of Differential Form C_D retrievals. Vertical black line highlights $u_m = -3$ m s^{-1} for clarity.

3.2.3 Optimized Form

If we can assume that u_m is always a constant -3 m s^{-1}, then $ILPI$ retrievals significantly improve (Fig. 3.14). The spread of noise is substantially reduced, and there is a decrease in spread of $ILPI$ retrievals as the CM1 C_D is increased. Plus, in contrast to Fig. 3.5, there is no longer a distinct high or low bias in $ILPI$ relative to v_{max}. There are also no more negative $ILPI$ retrievals, which is likely more consistent with the relatively modest fluctuations in v_{max}.

In addition to improvements in $ILPI$, similar improvements can be seen in C_D retrievals when assuming $u_m = -3$ m s^{-1}, and this form is hereafter referred as the Optimized Form (Fig. 3.15). While

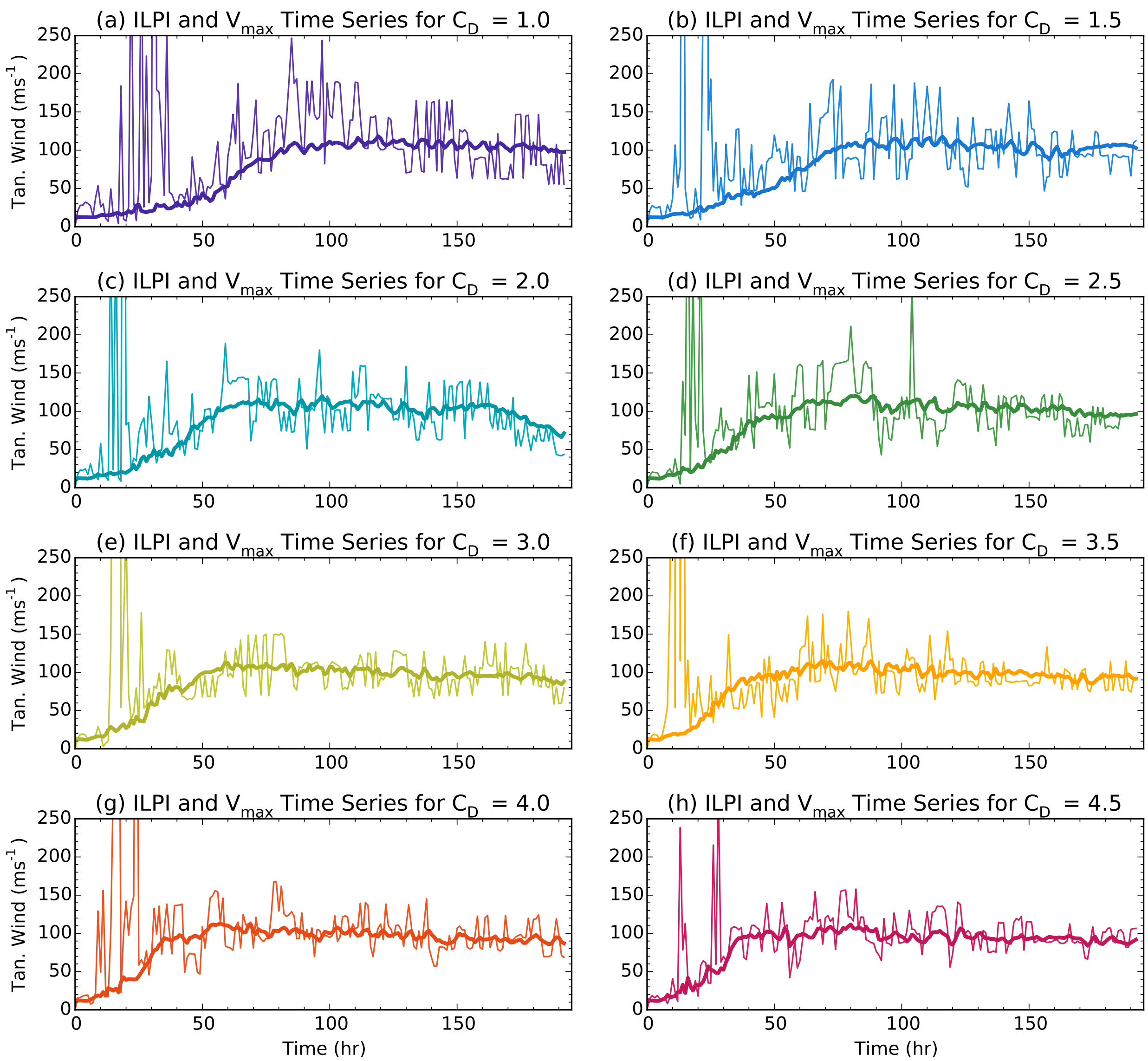

FIG. 3.14. As in Fig. 3.5, but for the Optimized Form of $ILPI$, where the Differential Form of $ILPI$ is recalculated assuming that $u_m = -3$ m s^{-1}.

the Optimized Form C_D retrieval variability is still proportional to the CM1 C_D magnitude, the spread is considerably reduced after the model spin-up period. In addition, there are no longer any unphysical, negative C_D values.

When looking at the normalized residuals for the Optimized Form of Eq. 2.18, the error is reduced by roughly half to within approximately 100% (Fig. 3.16). Looking more closely at how the remaining terms affect error, Fig. 3.16 shows that the relationships discussed for the Differential Form are even more apparent with the reduced degree of freedom. The inverse relationship of z_m and α^2 is more apparent, where a higher z_m corresponds with a smaller α^2 (Fig. 3.16a-b). Therefore, as C_D increases, the v_{10} wind

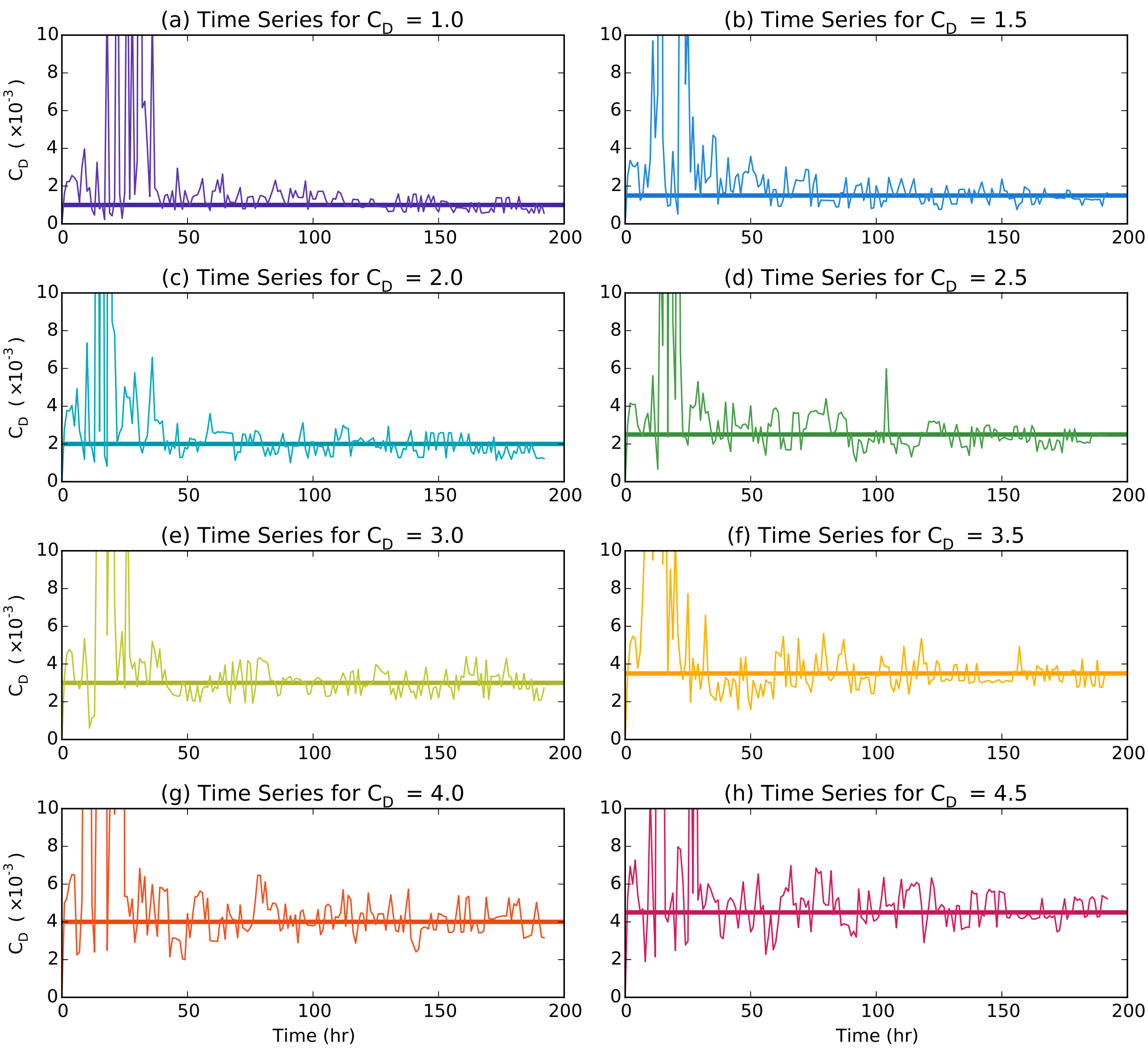

FIG. 3.15. As in Fig. 3.6, for the Optimized Form of C_D retrievals, where C_D is recalculated assuming that $u_m = -3$ m s^{-1}.

is decreased more, such that there is an increased difference between the magnitudes of v_{max} and v_{10}. The increased agradient torque from increased surface friction then forces v_{max} to increase in height.

While r_m and v_{max} also have a clear inverse relationship with each other (Fig. 3.16c-d), there is not as clear of a trend as C_D increases. Low r_m are associated with both positive and negative error, but it appears that r_m in excess of 30 km generally are associated with less error than smaller r_m. While this may possibly suggest an "optimal" r_m for retrievals, the more likely explanation is that the relatively coarse grid spacing is introducing some error.

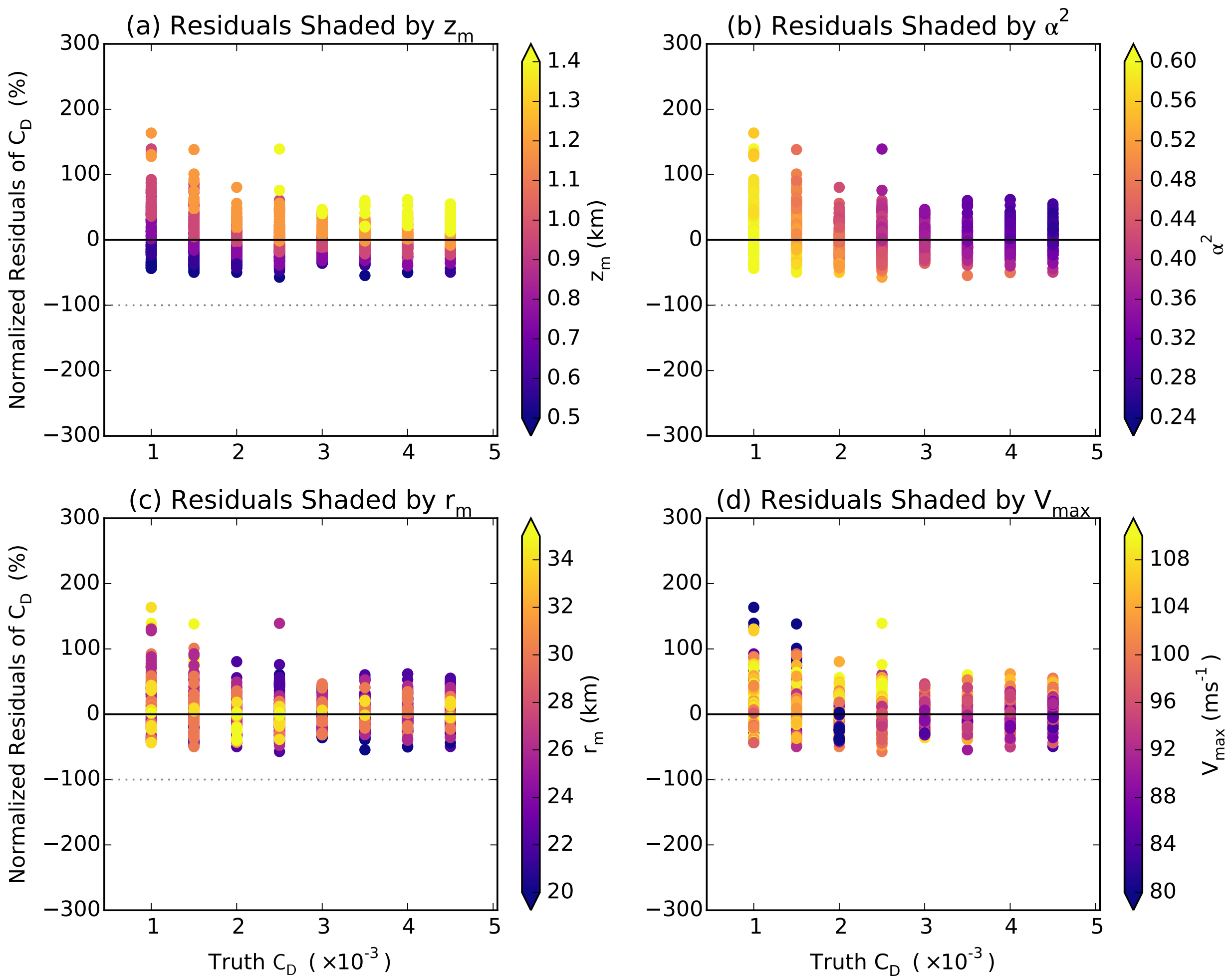

FIG. 3.16. Normalized residuals of the Optimized Form of C_D, where u_m is set to a constant −3 m s^{-1}. Shading denotes: (a) z_m (km), (b) α^2, (c) r_m (km), and (d) v_{max} (m s^{-1}).

As in Fig. 3.12, the normalized residuals decrease in magnitude for the Optimized Form (Fig. 3.17). However, there are no longer any appreciable biases, and averaging over 24 hr increments has a maximum error of approximately 50% for $C_D = 1$. Since the maximum error for the 24 hr averages for C_D = 1 is slightly over 100% without the $u_m = -3$ m s^{-1} assumption, then error is roughly halved when incorporating the assumption.

When we look at the nondimensional components of the Optimized Form C_D retrievals in log space, it is clear that α^2 plays a dominant role (Fig. 3.18). However, α^2 is not a sufficient variable by itself, because it increasingly underestimates C_D as the CM1 C_D is increased. Thus, v_{max} and its radial and vertical position become increasingly important for accurate C_D retrievals as C_D is increased, and as expected from Fig. 3.16, z_m is particularly important for offsetting α^2.

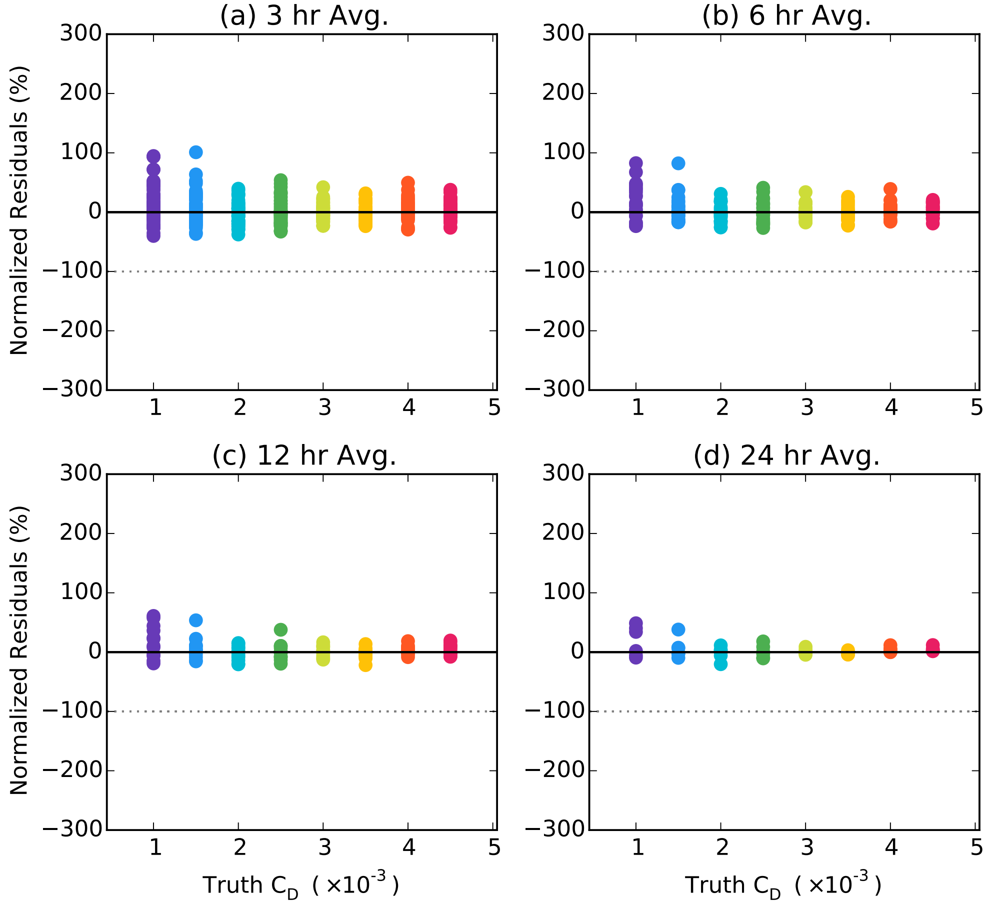

FIG. 3.17. As in Fig. 16, but for the Optimized Form of C_D retrievals.

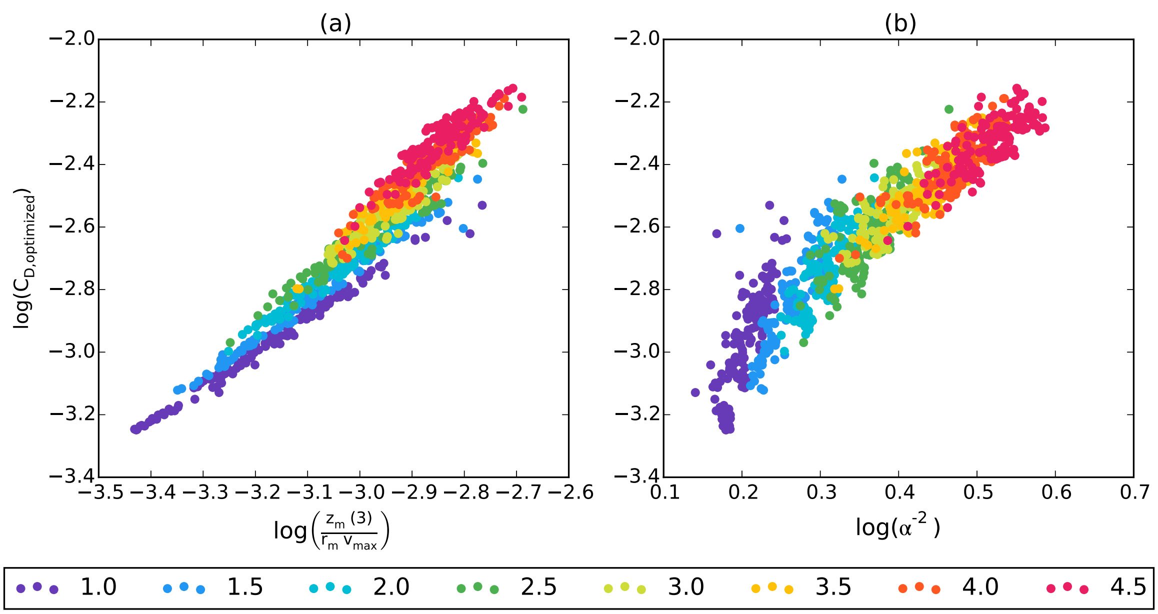

FIG. 3.18. Relationship between (a) $\log\left(\frac{z_m(3)}{r_m v_{max}}\right)$, and (b) $\log(\alpha^{-2})$, vs. $\log\left(C_{D,Optimized}\right)$.

While assuming $u_m = -3$ m s^{-1} results in optimal C_D retrievals for this axisymmetric model setup, it may or may not be appropriate to generalize this assumption to other models or observations. Therefore, the remainder of this study is to explore its generality.

3.3 Experiment 3: Sensitivity to Varying L_h and L_v

To determine if the $u_m = -3$ m s^{-1} assumption is a general, physical result or just the result of the particular model setup used in this study, a brief sensitivity study is performed. Specifically, only the sensitivity to the horizontal and vertical turbulent mixing lengths, L_h and L_v, are tested in this study because they have previously been shown to have a substantial effect on TCBL structure (e.g. Bryan and Rotunno 2009; Smith and Thomsen 2010; Rotunno and Bryan 2012; Zhang et al. 2018), While a variety of factors—such as model choice, grid spacing, and other various boundary layer parameterizations—likely also affect TCBL structure and the magnitude of u_m, testing all possible sensitivities is outside the scope of this study.

To test the effects of L_h and L_v on u_m, additional axisymmetric CM1 simulations were performed where C_D and C_K were both held constant at $C_D = C_K = 2.5$, and the turbulent mixing lengths from the Experiment 2 $C_D = 2.5$ simulation (hereafter the control simulation) were either halved or doubled, as described in Section 2.2 and Fig. 2.4.

Before examining the effects of L_h and L_v on the retrievals, the Experiment 3 v_{max} time series show substantial reductions in v_{max} as L_h increases, especially when the TCs are becoming quasi-steady around $t = 70$ hr (Fig. 3.19). However, there does not appear to be a discernible difference in intensification rate of v_{max} as L_v is increased, which contrasts with the findings of Zhang et al. (2018). Interestingly, after $t = 150$ hr, all of the v_{max} time series appear to converge towards $v_{max} \approx 95$ m s^{-1}.

The 114-120 hr averaged TCBL structure for the sensitivity study is shown in Fig. 3.20, and results are consistent with those of Rotunno and Bryan (2012) in the sense that increasing L_h decreases v_{max}, but there is not a clear relationship with tangential wind magnitudes when L_v is increased. However, while there is not a distinct relationship with the tangential wind magnitudes, increasing L_v does increase the slope of the tangential wind contours, such that they become more vertically oriented. In addition, both the radius and height of the approximate v_{max} show slight evidence of increasing with either increasing L_h and L_v, such that the largest horizontal and vertical turbulent mixing lengths result in the largest r_m and z_m.

When looking at the 6-hour averaged radial wind, Fig. 3.20 shows that there is a slight increase in the maximum radial inflow as L_h is increased, but a decrease when L_v is increased. In addition, as

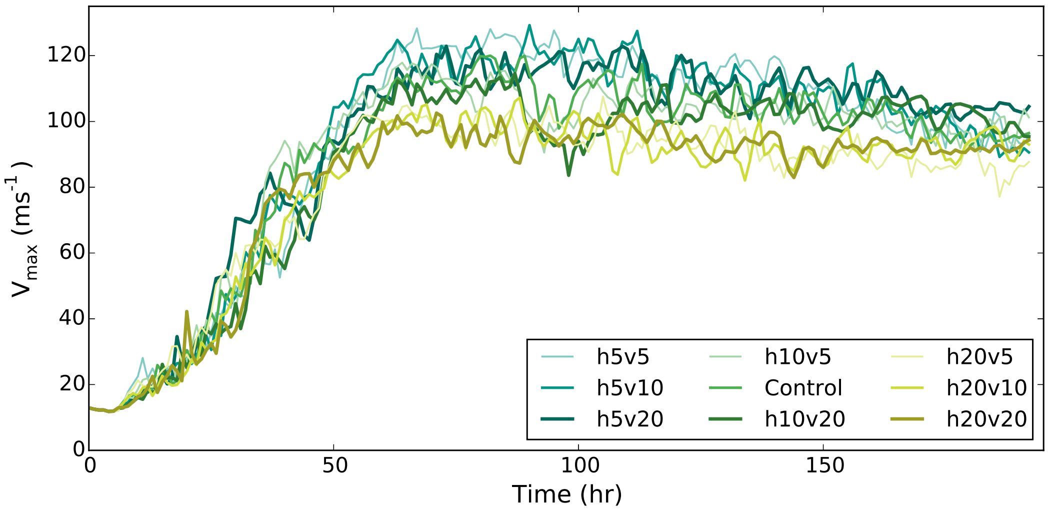

FIG. 3.19. As in Fig. 3.2, but for Experiment 3.

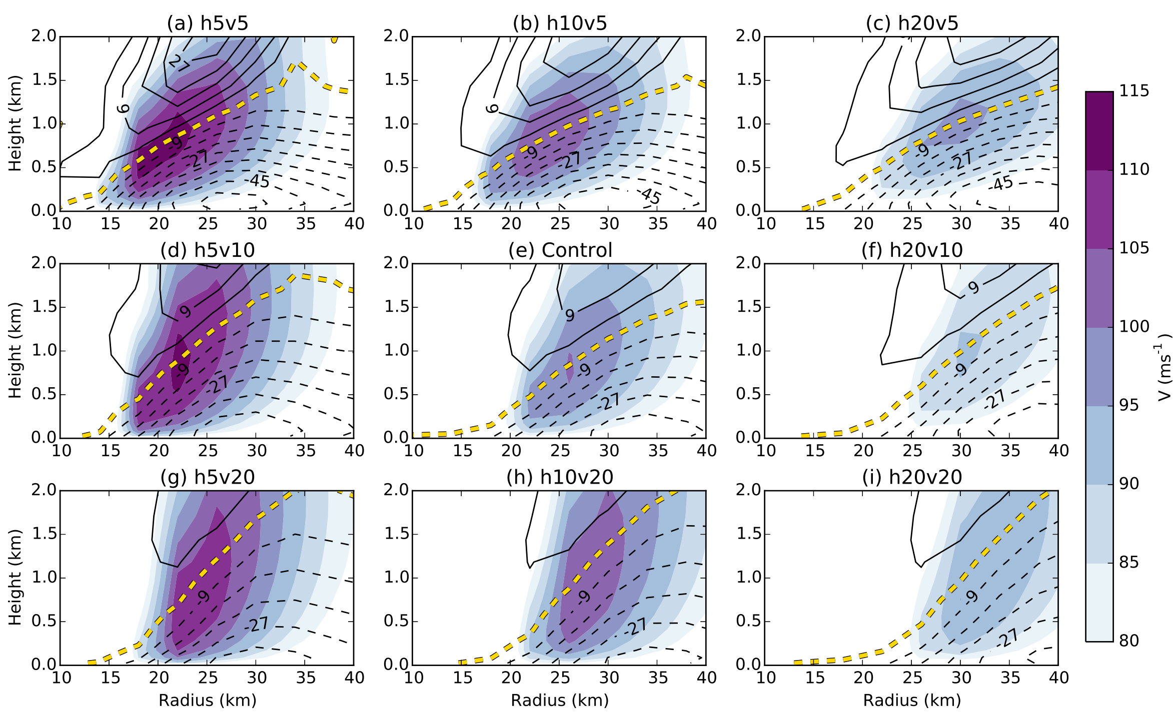

FIG. 3.20. As in Fig. 3.3, but for Experiment 3.

L_h is increased, the maximum inflow shifts radially outward from the tangential wind maximum, but stays proportionally similarly located when L_v is increased. The slope of the $u = -3$ m s^{-1} radial wind contour also increases for increasing L_v, but stays similar for L_h. Interestingly, the maximum tangential wind contour is nearly bisected by the $u = -3$ m s^{-1} contour for $L_v = 50$ m and $L_v = 100$ m, but the maximum tangential wind contour is situated closer to the surface such that it is not bisected in half any more when $L_v = 200$ m.

All together, Fig. 3.20 suggests that the horizontal and vertical mixing lengths modify the TCBL structure in ways that may affect the conceptual framework proposed in this study. Thus, further investigation is warranted to determine if the conceptual framework is highly specific to the modified TCBL structure from the turbulent mixing lengths.

Looking more specifically at u_m, results show that there is greater sensitivity to L_v (Fig. 3.21a). In particular, the spread of u_m decreases by almost half when L_v is increased from 50 m to 200 m, and the mean u_m after model spin-up also becomes increasingly negative as well. However, while there is no consistent trend in the means of u_m as L_h is increased, the spread of u_m decreases slightly with increasing L_h. This is expected because increasing the turbulent mixing length decreases the gradient through larger turbulent eddies and increased mixing, and the gradient of the radial wind is much larger in the vertical than the horizontal. As a result, there is greater sensitivity to the vertical turbulent mixing length.

In contrast to u_m, α^2 is much more sensitive to L_h than L_v (Fig. 3.21c). However, L_h and L_v affect α^2 in different ways. Increasing L_h decreases α^2 such that the vertical tangential wind gradient is increased between v_{max} and v_{10}, but increasing L_v increases α^2 such that this gradient is reduced. In addition, increasing L_v dramatically decreases the spread of α^2 magnitudes. This decrease in spread and increase in α^2 when increasing L_v is also expected because the tangential wind gradient is larger in the vertical rather than the horizontal, which results in larger sensitivity to the vertical turbulent mixing length. The decrease in α^2 as L_h is increased is interesting, and may be a result from the wider turbulence eddies interacting with the ocean surface over longer distances, which would then further decrease v_{10}.

In contrast, both r_m and z_m exhibit different relationships than u_m and α^2 (Fig. 3.21b, d). Both r_m and z_m increase with an increase in both L_h and L_v, which makes sense because larger turbulent eddies result in a larger TCBL. Interestingly, while increasing L_v decreased the spread in u_m and α^2, increasing L_v does not have as much of an effect on the spreads of r_m and z_m.

Therefore, the different terms of $ILPI$ and C_D are sensitive to L_h and L_v in different ways. The radial inflow at v_{max} becomes increasingly negative as L_v is increased and less variable as L_h is increased. The difference between v_{max} and v_{10} becomes smaller with increasing L_v, but larger with increasing L_h. Finally, the radius and height of v_{max} both become larger with increasing L_h and L_v.

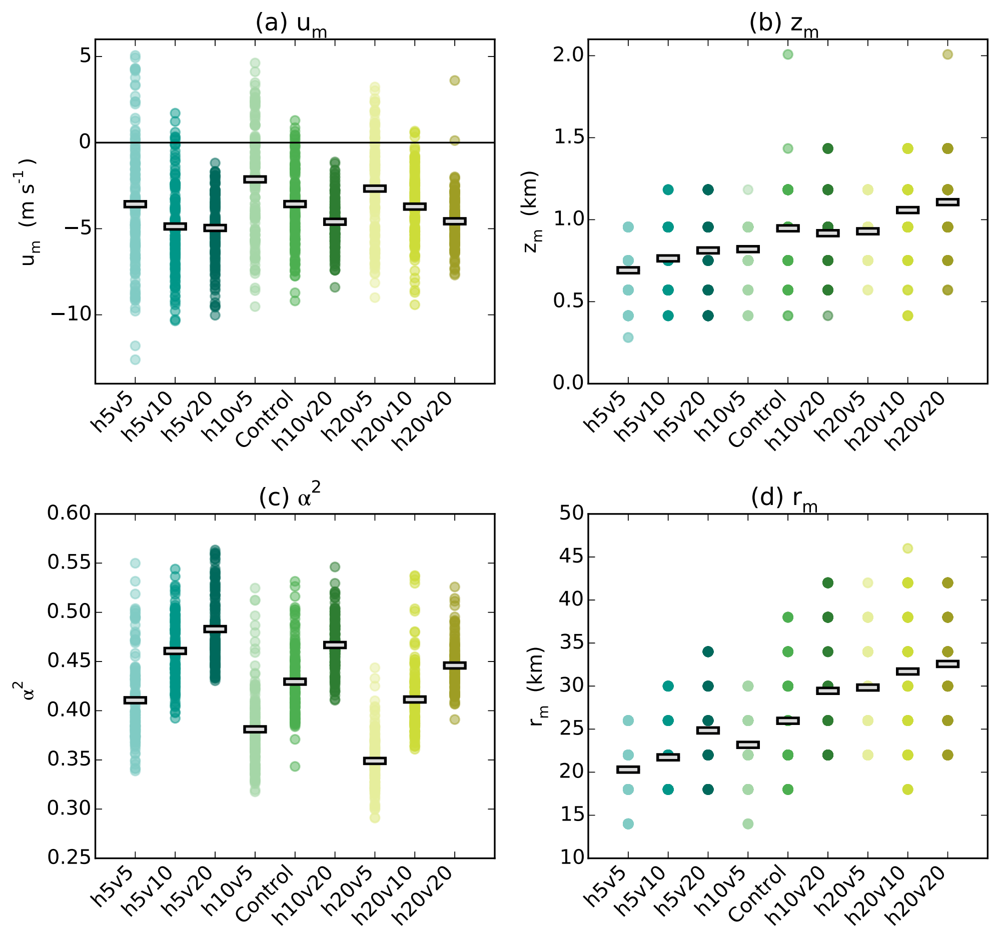

FIG. 3.21. Values and means of (a) u_m, (b) z_m, (c) α^2, and (d) r_m as in Fig. 3.4, but for Experiment 3. Note the different y-axis for u_m.

When examining how changing L_h and L_v affects the $ILPI$ in Eq. 2.13, results show that the $ILPI$ variability is substantially reduced as L_v is increased (Fig. 3.22). However, there is not an appreciable difference in the spread of $ILPI$ as L_h is increased. Interestingly, as L_v is increased, there is also a pronounced overshoot of $ILPI$ compared to v_{max} when the TCs are becoming quasi-steady.

Similarly, the Differential Form of C_D retrievals also show similar trends to $ILPI$ when L_h and L_v are modified (Fig. 3.23). There is less variability and fewer unphysical, negative retrievals as L_v is increased. In addition, there are much less apparent differences as L_h is increased, which suggests that the Differential Form of C_D is more sensitive to L_v than L_h in this framework.

Closer examination of the normalized residuals of both the Differential Form of C_D residuals confirm what the C_D time series qualitatively indicate; the spread of C_D retrievals are more sensitive to changes in L_v than L_h (Fig. 3.24a). However, the Optimized Form of C_D residuals actually indicates the opposite

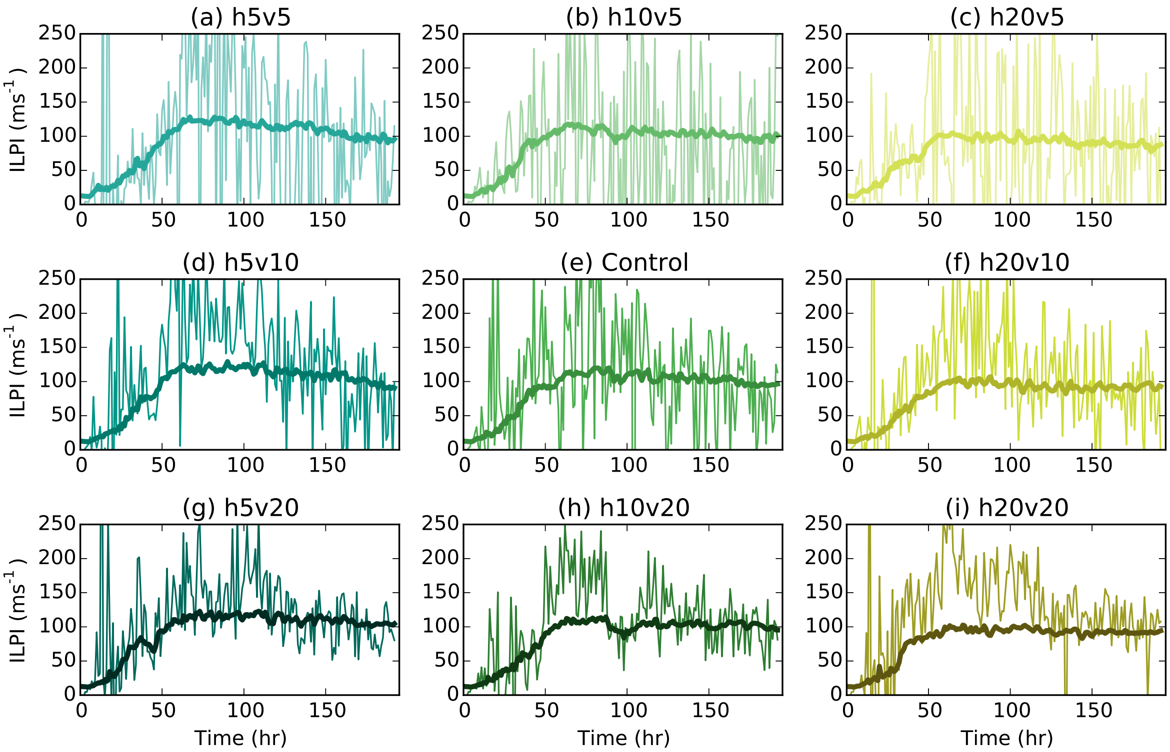

FIG. 3.22. As in Fig. 3.5, but for Experiment 3.

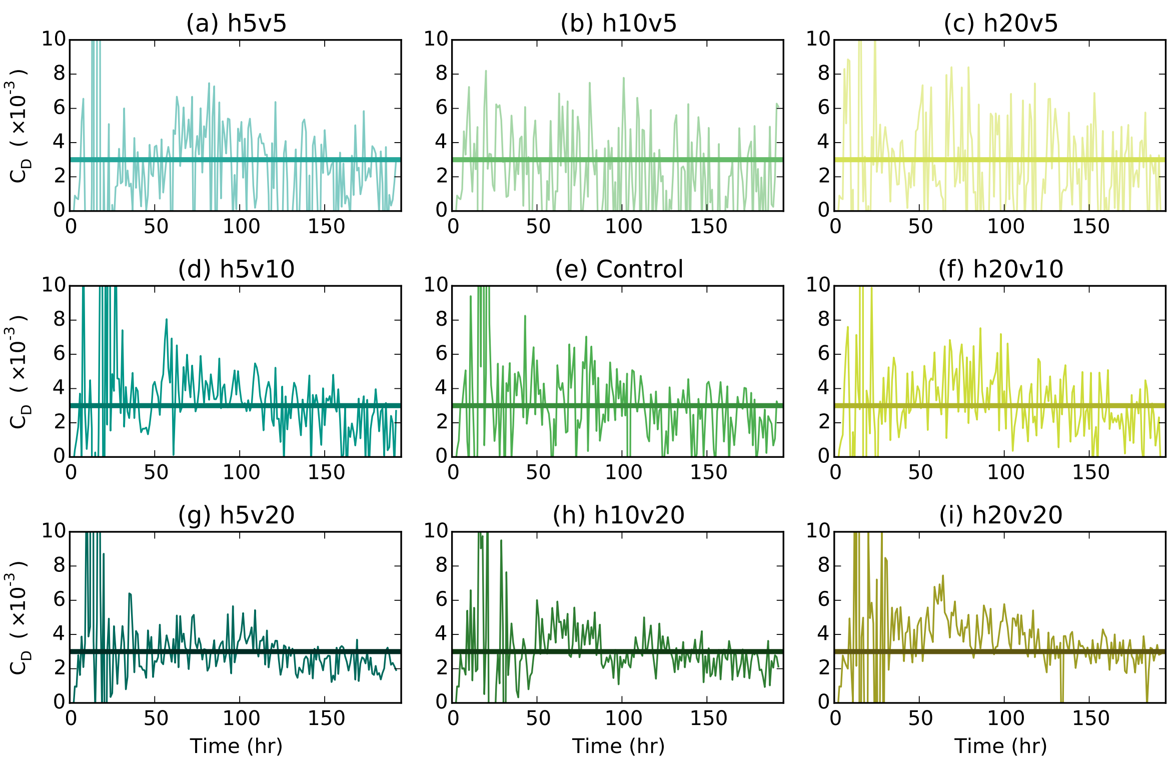

FIG. 3.23. As in Fig. 3.6, but for Experiment 3.

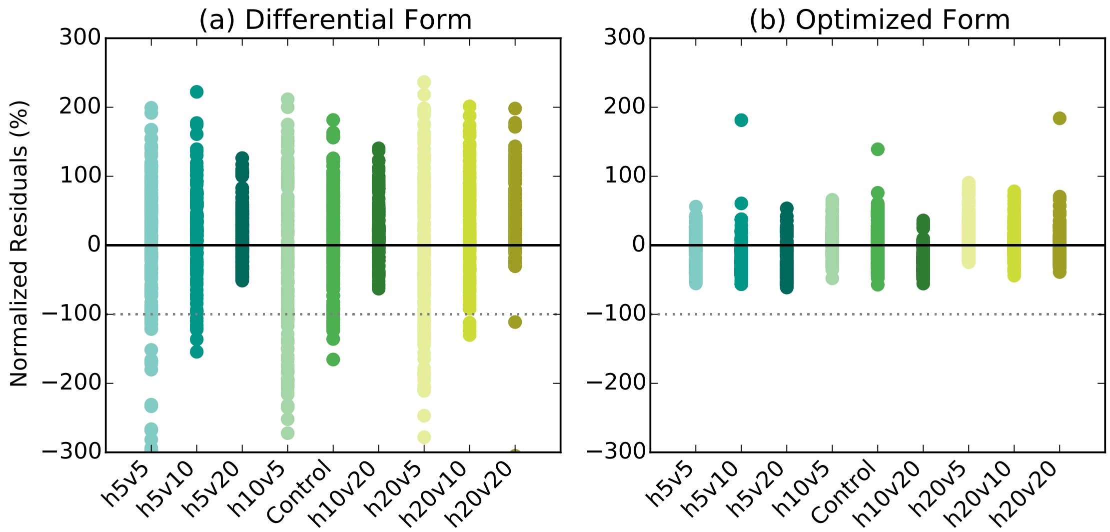

FIG. 3.24. Normalized residuals of C_D as in Fig. 3.11b and Fig. 3.16, but for Experiment 3.

effect; when assuming $u_m = -3$ m s^{-1}, the range of residuals becomes similar for all simulations at approximately 55%, but the bias shifts to be increasingly positive as L_h is increased from lower values in the shades of blue to higher values in the shades of yellow (Fig. 3.24b). This suggests that the Optimized Form of C_D residuals can mitigate sensitivity to L_v to an extent, but not L_h.

When the Differential Form of C_D retrievals are averaged over the same previous time intervals, results show that in addition to a decrease in variability as L_v is increased, there is also a systematic positive shift in bias (Fig. 3.25). However, there is not a systematic change in bias as L_h is increased for a given L_v. Thus, temporally averaging the Differential Form of C_D retrievals to reduce uncertainty is also sensitive to L_v.

If we look at the relationship between u_m and the normalized Differential Form of C_D residuals directly, results show that the distribution of inflow at v_{max} increases as L_v increases (Fig. 3.26). In addition, the approximate slope of the relationship becomes less steep as L_v increases, but it becomes slightly more steep as L_h increases. However, while there are slight differences in the approximate zero-error intercept of u_m, the differences are not substantial. Thus, a more general optimal u_m assumption is likely in the range from -3 to -5 m s^{-1}, depending on the turbulent mixing lengths that are in use.

Overall, Experiment 3 shows that the assumption of $u_m = -3$ m s^{-1} is not a general solution, because it is not entirely appropriate for all turbulent mixing lengths. However, assuming a constant u_m reduces a degree of freedom, which reduces the spread of retrieved $ILPI$ and C_D. In addition, while retrievals are

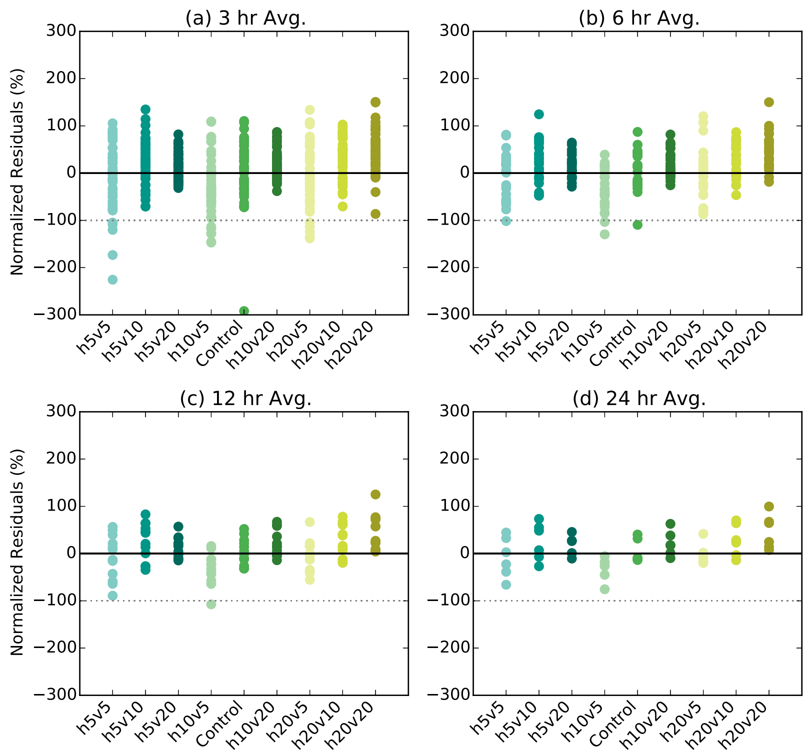

FIG. 3.25. As in Fig. 3.12, but for Experiment 3.

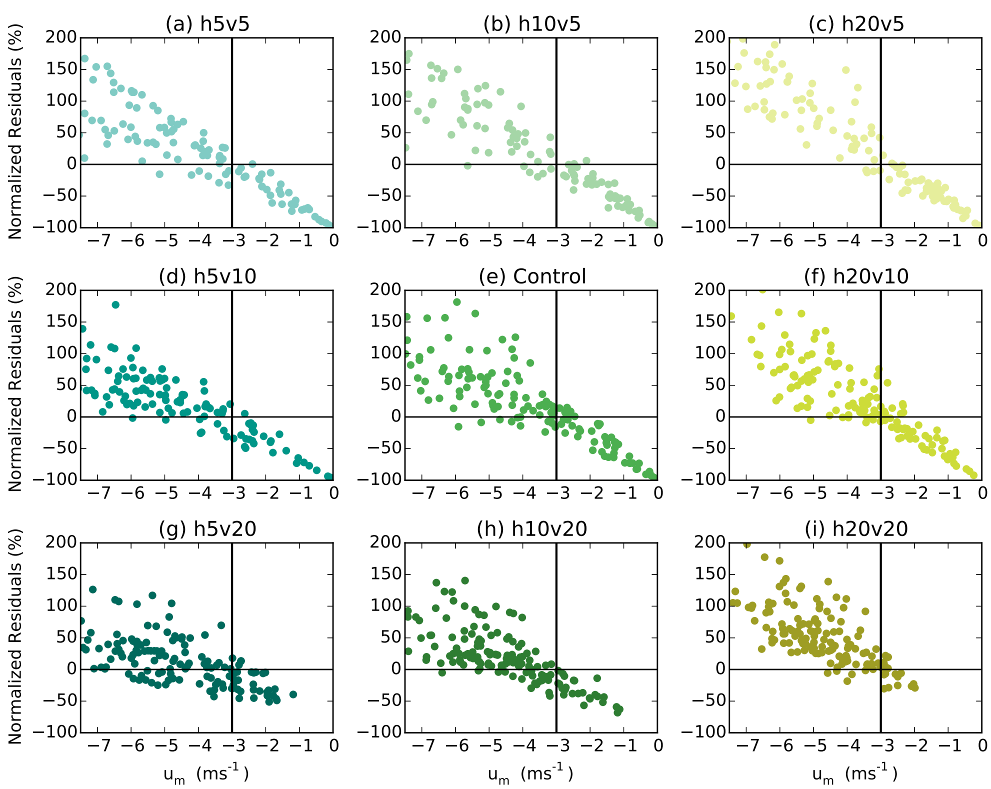

FIG. 3.26. As in Fig. 3.13, but for Experiment 3.

sensitive to turbulent mixing lengths, assuming a constant u_m drastically reduces this sensitivity. Thus, there may be different u_m that are appropriate for different situations.

3.4 Observations

Since the new LGE framework appears to be consistent with the TCBL characteristics seen in CM1, its applicability to observations is also explored. Therefore, to test the LGE framework with TCBL observations, SAMURAI analyses were constructed for Hurricane Joaquin (2015) from TCI dropsondes from $2-5$ Oct 2015, and they show somewhat different TCBL structure from the idealized CM1 simulations. Comparing Hurricane Joaquin's TCBL with the CM1-modeled TCBL, the most clear difference is that Hurricane Joaquin's maximum tangential winds on all four days are much weaker than the modeled CM1 winds (Fig. 3.27). In addition, the maximum radial inflow is also much weaker for all four days as well.

However, even though the maximum radial inflow is much weaker than any of the CM1 simulations, u_m is surprisingly similar for most of Hurricane Joaquin's analyses. Two of the days are close to $u_m = -3$ m s^{-1}; $u_m = -3.3$ m s^{-1} and $u_m = -3.7$ m s^{-1} on 2 Oct 2015 and 4 Oct 2015, respectively (Fig. 3.27a, c). In addition, on 5 Oct 2015, a secondary tangential wind maximum appears to be forming along the $u = -3$ m s^{-1} contour at approximately a radius of 90 km (Fig. 3.27d).

In contrast, on 3 Oct 2015, the analyzed u_m is actually marginally positive at $u_m = 0.6$ m s^{-1} (Fig. 3.27b). As a result, the Differential Form of $ILPI$ and C_D would be negative. Since the v_{max} that occurs 24 hours later is decreased by approximately 20 m s^{-1}, a negative $ILPI$ may be justified. However, the Differential Form of C_D would still not be applicable for this day because it would yield an unphysical, negative result.

Similar to Hurricane Joaquin, Hurricanes Fabian (2003) and Isabel (2003) also have u_m that are reasonably close to -3 m s^{-1}. Hurricane Fabian has $u_m = -5.98, -1.07$, and -3.19 m s^{-1} from $2-4$ Sep 2003, respectively, and Hurricane Isabel has $u_m = -2.60, -5.82$, and -4.39 m s^{-1} from $12-14$, respectively. Therefore, the average u_m for the three flights of Hurricane Fabian is -3.41 m s^{-1}, and -4.27 m s^{-1} for Hurricane Isabel.

Calculating the Differential and Optimized Forms of C_D for Hurricanes Joaquin, Fabian, and Isabel yield Fig. 3.28. Results show that there is not a discernible relationship between the Differential Form of C_D with the 10-m horizontal wind speed (Fig. 3.28a). However, when assuming $u_m = -3$ m s^{-1}, the Optimized Form of C_D does exhibit a possible negative relationship with respect to the 10-m wind speed

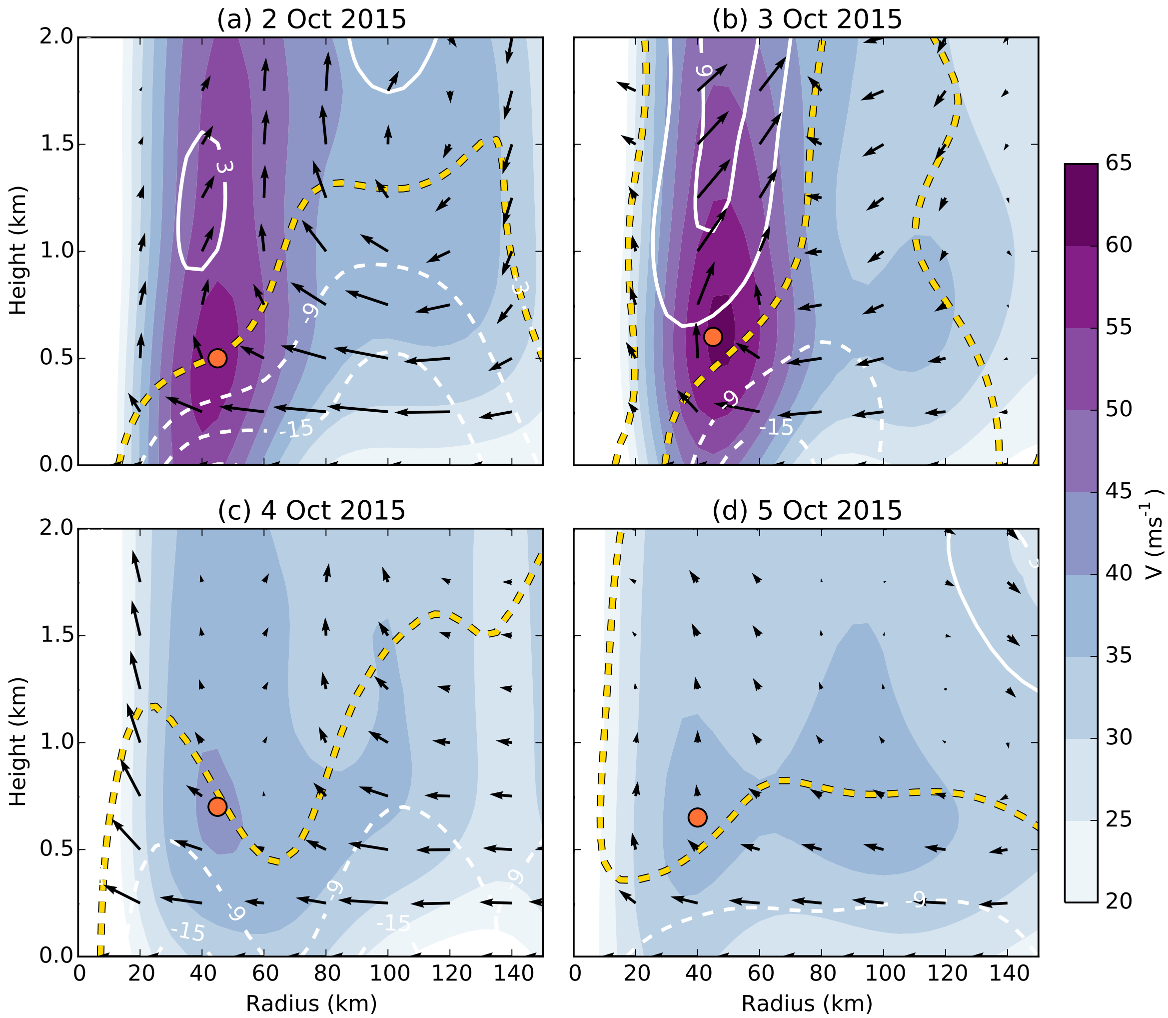

FIG. 3.27. SAMURAI analyses of Hurricane Joaquin from 2 – 5 Oct 2015, where: shading denotes tangential wind (m s^{-1}) starting at 20 m s^{-1}, contours denote the radial wind every 6 m s^{-1}, and arrows denote the secondary circulation, where the vertical velocity component has been enhanced by a factor of 30. The maximum tangential wind for each analysis is denoted by the orange point.

(Fig. 3.28b). In addition, the spread of the Optimized Form of C_D retrievals also decreases by approximately half when comparing to the Differential Form. Furthermore, the stronger 10-m horizontal wind speeds tend to be associated with the smallest Optimized Form of C_D for each TC, and the Optimized C_D for each of the three TCs tends to increase after the peak observed intensity.

Interestingly, Fig. 3.28b visually resembles the relationship proposed in Makin (2005, Fig. 1a). However, Fig. 3.28b is comparatively lower, and the small number of data points limits the definitiveness of conclusions. For example, if the highest Optimized C_D on 4 – 5 Oct 2015 are removed from the analysis, the relationships are not nearly as similar.

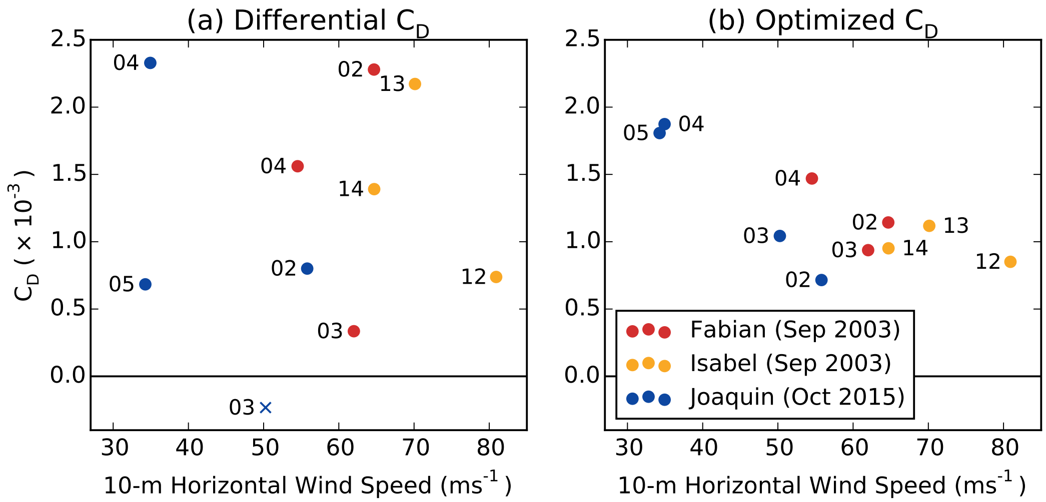

FIG. 3.28. Differential and Optimized Forms of C_D retrievals for: (red) Hurricane Fabian (2003); (gold) Hurricane Isabel (2003); and (blue) Hurricane Joaquin (2015) plotted with respect to the 10-m horizontal wind speed (m s^{-1}). Numbers on the points refer to the day of the axisymmetric analysis. The Joaquin analysis on 3 Oct 2015 yields an unphysical, negative result for the Differential Form of C_D; thus, it is represented with an X. The analyses of Hurricanes Fabian and Isabel can be found Bell et al. (2012).

While the bias of the Optimized Form of C_D could potentially be adjusted by fine-tuning the optimal u_m to better match Makin (2005), an important consideration is that there is also uncertainty introduced from the analysis procedure. In particular, the Gaussian filter length chosen for SAMURAI would affect the results of this study. Thus, definitive conclusions cannot be made about either of the C_D retrievals without further sensitivity testing, which is beyond the scope of this study.

When directly comparing the C_D results of Hurricanes Fabian and Isabel to the previous method proposed in Bell et al. (2012) and to the rest of the C_D estimates seen in Soloviev et al. (2017), results show that the method proposed in this study are comparatively low (Fig. 3.29). However, for most analyses, this study's results are within two standard deviations of those found in Bell et al. (2012), and half of the Optimized Form of C_D retrievals lie within the 95% confidence intervals found in Bell et al. (2012). Interestingly, the Optimized values also appear to extend the general pattern of the upper ocean current response of Jarosz et al. (2007).

Overall, while observations of TCBL structure and C_D are limited, the initial results of this study potentially indicate that C_D may be lower than previous estimates for TC surface wind speeds. In addition, analyses of Hurricane Joaquin indicate that $u_m = -3$ m s^{-1} is not an unreasonable assumption. However, more observational axisymmetric analyses across TC intensities are still needed to adequately justify this assumption and quantify observed variability of C_D.

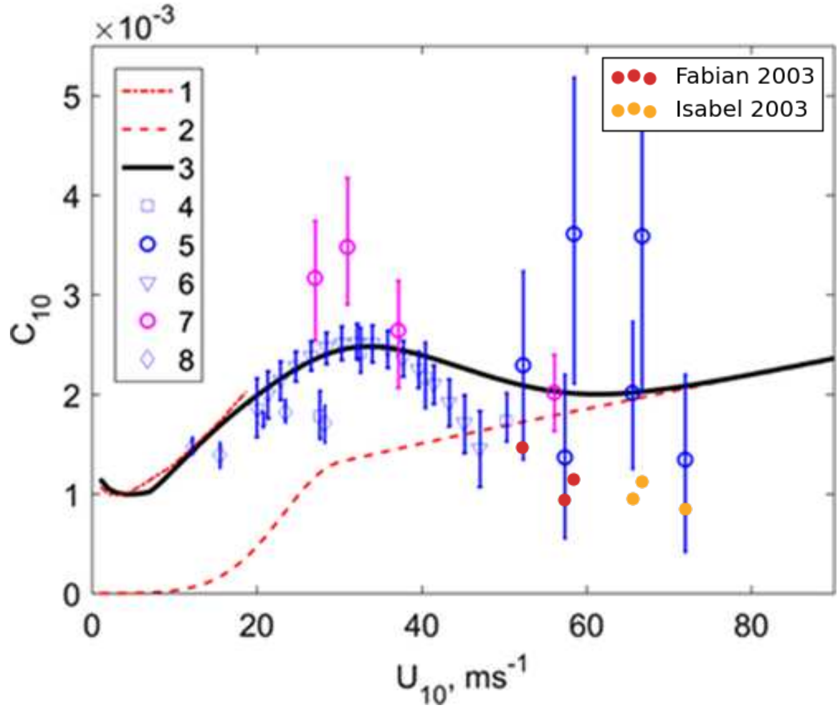

FIG. 3.29. As in Fig. 1.1, but with the Optimized Form of C_D retrievals for Hurricanes Fabian and Isabel overlaid. Retrievals are horizontally translated to the domain-average horizontal 10-m wind speed found in Bell et al. (2012) for each analysis to aide in comparisons with the 95% confidence intervals.

CHAPTER 4

Conclusions

The TCBL is a unique and important part of tropical cyclones, due to its clear importance for both TC intensification and societal impacts. However, it is also currently one of the least understood parts of a TC due to its complex, nonlinear nature, as well as the hazards associated with collecting in situ measurements, such as TCBL structure or the magnitude of C_D within it. Therefore, to address and simplify some complexities of the TCBL, the relationships between TCBL structure and TC intensity have been explored through the lens of a new, nonlinear conceptual framework that is derived from first principles with a logistic growth equation. This conceptual framework introduces a vortex-based potential intensity metric—the instantaneous logistic potential intensity, $ILPI$—which is based on: the radial inflow at the location of the axisymmetric tangential wind speed maximum, u_m; the approximate depth of the TCBL, z_m; the vertical tangential wind speed gradient between the axisymmetric tangential wind speed maximum and the axisymmetric 10-m tangential wind speed, $\alpha^2 = (v_{max}/v_{10})^2$; the radius of v_{max}, r_m; and the drag coefficient, C_D. The conceptual relationships between these individual variables and $ILPI$ are depicted in Fig. 2.1.

Mathematically, the $ILPI$ in Eq. 2.13 shows that a more negative u_m, which implies stronger inflow at the location of v_{max}, would indicate a higher potential intensity. A large z_m would indicate a deeper inflow layer, and it would also increase the potential intensity. In the denominator, a smaller r_m could increase the potential intensity, as well as a reduced C_D. In addition, a smaller α^2 implies a larger vertical tangential wind gradient between v_{max} and v_{10} at r_m, and a larger vertical tangential wind gradient would imply a larger potential for intensification.

While these processes have been presented separately for conceptual understanding in this study, it is important to note that they all interact simultaneously and can lead to competing intensification trends. For example, an increase in C_D would result in a weaker TC by itself, but it also leads to a decreased α^2 by torquing more tangential wind into the radial component, which then acts to intensify a TC in the short term. In addition, this study showed that an increased C_D corresponded with an increased z_m and a decreased r_m, which would both also counteract TC weakening. Therefore, increasing C_D has multiple secondary effects that act to intensify a TC in spite of the direct effect, which is consistent with the increased intensification rates shown in this and the previous studies of Bao et al. (2012), Green and Zhang (2014), Montgomery et al. (2010), and Smith et al. (2014) as C_D is increased.

Since C_D is shown to systematically result in the TCBL structural changes that are depicted in Fig. 2.1, this conceptual framework is also extended to retrieve the drag coefficient directly from TCBL structure, and several ways to retrieve C_D were explored. While the Integral Form is exact and does not require additional assumptions, the approximate Differential Form is preferred in this study due to its simplicity while retaining skill. In exploring the Differential Form, results suggest that v_{max} is preferentially located along a specific u_m, and in the axisymmetric CM1, this value was $u_m = -3$ m s^{-1}. Sensitivity of this u_m value to the horizontal and vertical turbulent mixing lengths is also explored, and while there is sensitivity to both quantities, u_m and C_D do not immensely change. For both the Differential and Optimized Forms, a doubled L_h from the control results in a slightly positive shift of approximately 10%, and halving it results in no appreciable change. However, while changing L_v has no appreciable effect on the Optimized Form, doubling L_v decreases the spread of the Differential Form to within approximately 200% and halving L_v increased the spread to within approximately 300%.

In addition to the modeling proof-of-concept, retrieving C_D from TCBL structure also has applications for observations. Directly observing the 10-m wind speed in a major TC remains challenging for existing observational methods, which highly contributes to the uncertainty of the magnitude of C_D for these wind speeds. Thus, indirectly observing C_D from TCBL structure is an appealing alternative, since TCBL structure can be more safely retrieved from airborne radar and dropsondes. While testing this method on observations is ongoing and future work, the results of this study indicate that most retrievals are on the order of $C_D = 1-2\times10^{-3}$ for the new analyses of Hurricane Joaquin (2015) and from the previous analyses of Hurricanes Fabian and Isabel (2003) from Bell et al. (2012). However, results also indicate that this retrieval method is sensitive to the analysis technique and distribution of observed data.

In conclusion, a new conceptual framework that links C_D to first principles has been proposed, and it bridges gaps in understanding the relationships between C_D, TCBL structure, and TC intensity change. It is consistent with the qualitative results of Montgomery et al. (2010) and Smith et al. (2014) on how C_D affects TCBL structure, and it expands on the second mechanism of TC intensification, which is associated with radial convergence within the TCBL and proposed by Smith et al. (2009), because in addition to radial convergence of relative angular momentum, this study also considers the effects of additional TCBL structural parameters, such as the TCBL height and radius of v_{max}. In addition, this conceptual framework is consistent with results of the axisymmetric version of CM1, and applying it towards C_D

retrievals from observations shows promise. Future work aims to better quantify the error characteristics of applying this new framework towards observations, as well as to further explore its sensitivities to different model setups.

REFERENCES

Bao, J. W., S. G. Gopalakrishnan, S. A. Michelson, F. D. Marks, and M. T. Montgomery, 2012: Impact of physics representations in the HWRFX on simulated hurricane structure and pressure-wind relationships. *Mon. Wea. Rev.*, **140**, 3278–3299, doi: 10.1175/MWR-D-11-00332.1.

Bell, M. M., M. T. Montgomery, and K. A. Emanuel, 2012: Air-sea enthalpy and momentum exchange at major hurricane wind speeds observed during CBLAST. *J. Atmos. Sci.*, **69**, 3197–3222, doi: 10.1175/JAS-D-11-0276.1.

Bell, M. M., et al., 2016: ONR Tropical Cyclone Intensity 2015 NASA WB-57 HDSS Dropsonde Data. Version 1.1. UCAR/NCAR - Earth Observing Laboratory, [Available online at: https://doi.org/10.5065/d6kw5d8m.] Accessed 23 Jan 2017.

Black, P. G., R. W. Burpee, N. M. Dorst, and W. L. Adams, 1986: Appearance of the sea surface in tropical cyclones. *Wea. Forecasting*, **1**, 102–107, doi: 10.1175/1520-0434(1986)001<0102:AOTSSI>2.0.CO;2.

Black, P. G., E. A. D'Asoro, J. R. French, P. P. Niller, S. T. B., E. J. Terril, E. J. Walsh, and J. A. Zhang, 2007: Air–sea exchange in hurricanes. synthesis of observations from the coupled boundary-layer air–sea transfer experiment. *Bull. Amer. Meteor. Soc.*, **88**, 357–374, doi: 10.1175/BAMS-88-3-357.

Bryan, G. H., 2012: Effects of surface exchange coefficients and turbulence length scales on the intensity and structure of numerically simulated hurricanes. *Mon. Wea. Rev.*, **140**, 1125–1143, doi: 10.1175/MWR-D-11-00231.1.

Bryan, G. H., 2013: Comments on "Sensitivity of tropical-cyclone models to the surface drag coefficient". *Quart. J. Roy. Meteor. Soc.*, **139**, 1957–1960, doi: 10.1002/qj.2066.

Bryan, G. H. and J. M. Fritsch, 2002: A benchmark simulation for moist nonhydrostatic numerical models. *Mon. Wea. Rev.*, **130**, 2917–2928, doi: 10.1175/1520-0493(2002)130<2917:ABSFMN>2.0.CO;2.

Bryan, G. H. and R. Rotunno, 2009: The maximum intensity of tropical cyclones in axisymmetric numerical model simulations. *Mon. Wea. Rev.*, **137**, 1770–1789, doi: 10.1175/2008MWR2709.1.

Bryan, G. H., R. P. Worsnop, J. K. Lundquist, and J. A. Zhang, 2017: A simple method for simulating wind profiles in the boundary layer of tropical cyclones. *Boundary Layer Meteor.*, **162**, 475–502, doi: 10.1007/s10546-016-0207-0.

Charnock, H., 1955: Wind stress on a water surface. *Quart. J. Roy. Meteor. Soc.*, **81**, 639–640, doi: 10.1002/qj.49708135027.

DeMaria, M., 2009: A simplified dynamical system for tropical cyclone intensity prediction. *Mon. Wea. Rev.*, **137**, 68–82, doi: 10.1175/2008MWR2513.1.

Donelan, M. A., B. K. Haus, N. Reul, W. J. Plant, M. Stiassnie, H. C. Graber, O. B. Brown, and E. S. Saltzman, 2004: On the limiting aerodynamic roughness of the ocean in very strong winds. *Geophys. Res. Lett.*, **31 (18)**, doi: 10.1029/2004GL019460.

Doyle, J. D., et al., 2017: A view of tropical cyclones from above: The Tropical Cyclone Intensity Experiment. *Bull. Amer. Meteor. Soc.*, **98**, 2113–2134, doi: 10.1175/BAMS-D-16-0055.1.

Emanuel, K. A., 1986: An air-sea interaction theory for tropical cyclones. part i: Steady-state maintenance. *J. Atmos. Sci.*, **43**, 585–605, doi: 10.1175/1520-0469(1986)043<0585:AASITF>2.0.CO;2.

Emanuel, K. A., 1995: Sensitivity of tropical cyclones to surface exchange coefficients and a revised steady-state model incorporating eye dynamics. *J. Atmos. Sci.*, **52**, 3969–3976, doi: 10.1175/1520-0469(1995)052<3969:SOTCTS>2.0.CO;2.

Emanuel, K. A., 2003: A similarity hypothesis for air–sea exchange at extreme wind speeds. *J. Atmos. Sci.*, **60 (11)**, 1420–1428, doi: 10.1175/1520-0469(2003)060<1420:ASHFAE>2.0.CO;2.

Fairall, C. W., E. F. Bradley, J. E. Hare, A. A. Grachev, and J. B. Edson, 2003: Bulk parameterization of air–sea fluxes: Updates and verification for the COARE Algorithm. *J. Climate*, **16**, 571–591, doi:

10.1175/1520-0442(2003)016<0571:BPOASF>2.0.CO;2.

Green, B. W. and F. Zhang, 2014: Sensitivity of tropical cyclone simulations to parametric uncertainties in air–sea fluxes and implications for parameter estimation. *Mon. Wea. Rev.*, **142**, 2290–2308, doi: 10.1175/MWR-D-13-00208.1.

Holthuijsen, L. H., M. D. Powell, and J. D. Pietrzak, 2012: Wind and waves in extreme hurricanes. *Geophys. Res. Lett.*, **117 (C9)**, doi: 10.1029/2012JC007983.

Hsu, J.-Y., R.-C. Lien, E. A. D?Asaro, and T. B. Sanford, 2017: Estimates of surface wind stress and drag coefficients in Typhoon Megi. *J. Phys. Oceanogr.*, **47**, 545–565, doi: 10.1175/JPO-D-16-0069.1.

Jarosz, E., D. A. Mitchell, D. W. Wang, and W. J. Teague, 2007: Bottom-up determination of air-sea momentum exchange under a major tropical cyclone. *Science*, **315**, 1707–1709, doi: 10.1126/science.1136466.

Kaimal, J. C. and J. C. Wyngaard, 1990: The Kansas and Minnesota experiments. *BLM*, **50**, 31–47, doi: 10.1007/BF00120517.

Kepert, J. D., J. Schwendike, and H. Ramsay, 2016: Why is the tropical cyclone boundary layer not "well mixed"? *J. Atmos. Sci.*, **73**, 957–973, doi: 10.1175/JAS-D-15-0216.1.

Large, W. G. and S. Pond, 1981: Open ocean momentum flux measurements in moderate to strong winds. *J. Phys. Oceanogr.*, **11**, 324–336, doi: 10.1175/1520-0485(1981)011<0324:OOMFMI>2.0.CO;2.

Lorsolo, S., J. A. Zhang, F. Marks Jr., and J. Gamache, 2010: Estimation and mapping of hurricane turbulent energy using airborne doppler measurements. *Mon. Wea. Rev.*, **138**, 3656–3670, doi: 10.1175/2010MWR3183.1.

Makin, V. K., 2005: A note on the drag of the sea surface at hurricane winds. *Boundary Layer Meteor.*, **115**, 169–176, doi: 10.1007/s10546-004-3647-x.

Montgomery, M. T., R. K. Smith, and S. V. Nguyen, 2010: Sensitivity of tropical-cyclone models to the surface drag coefficient. *Quart. J. Roy. Meteor. Soc.*, **136**, 1945–1953, doi: 10.1002/qj.702.

Morrison, H., G. Thompson, and V. Tatarskii, 2009: Impact of cloud microphysics on the development of trailing stratiform precipitation in a simulated squall line: Comparison of one- and two-moment schemes. *Mon. Wea. Rev.*, **137**, 991–1007, doi: 10.1175/2008MWR2556.1.

Moss, M. S. and F. J. Merceret, 1976: A note on several low-layer features of Hurricane Eloise (1975). *Mon. Wea. Rev.*, **104**, 967–971, doi: 10.1175/1520-0493(1976)104<0967:ANOSLL>2.0.CO;2.

Powell, M. D., P. J. Vickery, and T. A. Reinhold, 2003: Reduced drag coefficient for high wind speeds in tropical cyclones. *Nature*, **422**, 279–283, doi: 10.1038/nature01481.

Rotunno, R. and G. H. Bryan, 2012: Effects of parameterized diffusion on simulated hurricanes. *J. Atmos. Sci.*, **69**, 2284–2299, doi: 10.1175/JAS-D-11-0204.1.

Smith, R. K. and M. T. Montgomery, 2010: Hurricane boundary-layer theory. *Quart. J. Roy. Meteor. Soc.*, **136**, 1665–1670, doi: 10.1002/qj.679.

Smith, R. K., M. T. Montgomery, and V. S. Nguyen, 2009: Tropical cyclone spin-up revisited. *Quart. J. Roy. Meteor. Soc.*, **135**, 1321–1335, doi: 10.1002/qj.428.

Smith, R. K., M. T. Montgomery, and G. L. Thomsen, 2014: Sensitivity of tropical-cyclone models to the surface drag coefficient in different boundary-layer schemes. *Quart. J. Roy. Meteor. Soc.*, **140**, 792–804, doi: 10.1002/qj.2057.

Smith, R. K. and G. L. Thomsen, 2010: Dependence of tropical-cyclone intensification on the boundary-layer representation in a numerical model. *Quart. J. Roy. Meteor. Soc.*, **136**, 1671–1685, doi: 10.1002/qj.687.

Soloviev, A. V. and R. Lukas, 2010: Effects of bubbles and sea spray on air–sea exchange in hurricane conditions. *Boundary Layer Meteor.*, **136**, 365–376, doi: 10.1007/s10546-010-9505-0.

Soloviev, A. V., R. Lukas, M. A. Donelan, B. K. Haus, and I. Ginis, 2014: The air-sea interface and surface stress under tropical cyclones. *Nature Scientific Reports*, **4**, 5306, doi: 10.1002/2017JC013435.

Soloviev, A. V., R. Lukas, M. A. Donelan, B. K. Haus, and I. Ginis, 2017: Is the state of the air-sea interface a factor in rapid intensification and rapid decline of tropical cyclones? *J. Geophys. Res.: Oceans*, **122**, 10 174–10 183, doi: 10.1002/2017JC013435.

Zhang, J. A., W. M. Drennan, P. G. Black, and J. R. French, 2009: Turbulence structure of the hurricane boundary layer between the outer rainbands. *J. Atmos. Sci.*, **66**, 2455–2467, doi: 10.1175/2009JAS2954.1.

Zhang, J. A., F. D. Marks, J. A. Sippel, R. F. Rogers, X. Zhang, S. G. Gopalakrishnan, Z. Zhang, and V. Tallapragada, 2018: Evaluating the impact of improvement in the horizontal diffusion parameterization on hurricane prediction in the operational Hurricane Weather Research and Forecast (HWRF) model. *Wea. Forecasting*, **33**, 317–329, doi: 10.1175/WAF-D-17-0097.1.

Zhang, J. A., R. F. Rogers, D. S. Nolan, and F. D. Marks, 2011: On the characteristic height scales of the hurricane boundary layer. *Mon. Wea. Rev.*, **139**, 2523–2535, doi: 10.1175/MWR-D-10-05017.1.